Sequential activity of CA1 hippocampal cells constitutes a temporal 1 memory map for associative learning in mice 2 3 Ming Ma^{1,9}, Fabio Simoes de Souza.^{1,2,9}, Gregory L. Futia³, Sean R. Anderson.⁴, Jose 4 Riguero ^{4,5}, Daniel Tollin^{4,5}, Arianna Gentile-Polese¹, Jonathan P. Platt⁶, Kira Steinke⁷, 5 Naoki Hiratani⁸, Emily A. Gibson^{3,5} and Diego Restrepo^{1,5,*} 6 7 8 ¹Department of Cell and Developmental Biology, University of Colorado Anschutz 9 Medical Campus, Aurora, CO, 80045, USA. 10 11 ²Center for Mathematics, Computation and Cognition, Federal University of ABC, Sao 12 Bernardo do Campo, SP, Brazil. ³Department of Bioengineering, University of Colorado Anschutz Medical Campus, 13 14 Aurora, CO, 80045, USA. ⁴Department of Physiology and Biophysics, University of Colorado Anschutz Medical 15 16 Campus, Aurora, CO, 80045, USA. ⁵Neuroscience Graduate Program, University of Colorado Anschutz Medical Campus, 17 18 Aurora, CO 80045, USA. ⁶Department of Neurosurgery, University of Colorado Anschutz Medical Campus, 19 Aurora, CO, 80045, USA. 20 ⁷Integrated Physiology Graduate Program, University of Colorado Anschutz Medical 21 22 Campus, Aurora, CO, 80045, USA. ⁸Department of Neuroscience, Washington University, St. Louis, MO 63110, USA 23 24 25 ⁹These authors contributed equally to this work 26 27 *Lead contact: diego.restrepo@cuanschutz.edu 28 29 30 Keywords: hippocampus; decision-making; go-no go; associative learning; olfactory; 31 time cells

SUMMARY

Sequential neural dynamics encoded by "time cells" play a crucial role in hippocampal function. However, the role of hippocampal sequential neural dynamics in associative learning is an open question. We used two-photon Ca²+ imaging of dorsal CA1 (dCA1) neurons in the stratum pyramidale (SP) in head-fixed mice performing a go-no-go associative learning task to investigate how odor valence is temporally encoded in this area of the brain. We found that SP cells responded differentially to the rewarded or unrewarded odor. The stimuli were decoded accurately from the activity of the neuronal ensemble, and accuracy increased substantially as the animal learned to differentiate the stimuli. Decoding the stimulus from individual SP cells responding differentially revealed that decision-making took place at discrete times after stimulus presentation. Lick prediction decoded from the ensemble activity of cells in dCA1 correlated linearly with lick behavior indicating that sequential activity of SP cells in dCA1 constitutes a temporal memory map used for decision-making in associative learning.

INTRODUCTION

In the natural world, understanding and integrating sensory stimuli is essential for survival. An animal must be able to locate food and water, detect disease, avoid predators, and seek out mates to reproduce. Of note, the success of these behaviors relies heavily on the integration of olfaction¹ and experience² and is context-dependent. Thus, it is simply not enough for an animal to detect an odor; it must be able to also apply meaning to it (association) and then act accordingly. To accomplish this, the hippocampus provides real-time encoding and retrieval of detailed context memories enabling reactions to a constantly changing environment^{3,4}. Diverse and distributed neuronal activity encodes external features such as contextually referenced space and time and sensory stimuli, as well as features influenced by the animal's behavior such as speed and direction of motion⁵⁻⁸. Here we address the neural representation of associative learning in stratum pyramidale (SP) neurons of dorsal CA1 (dCA1), a hippocampal area involved in spatial learning and working memory tasks^{9,10}.

The involvement of dCA1 in associative learning of stimulus discrimination in head-fixed animals is still unclear¹¹⁻¹⁶. Li and co-workers showed that for mice engaged in an odor discrimination go-no go associative learning task dCA1 pyramidal cells receiving connections conveying olfactory information from the lateral entorhinal cortex (LEC) develop more selective spiking responses to odor cues as they learn to discriminate odorants. Importantly, they showed that optogenetic inactivation of the LEC to dCA1 connections slows learning¹⁶. In addition, Biane and colleagues found a learning-related

increase in the proportion of cells responsive to the rewarded (S+) odorant, but not to the unrewarded (S-) odorant, suggesting that stimulus representations in dCA1 are sensitive to perceived value. However, learning did not alter stimulus decoding accuracy which was already high before training in dCA1¹⁵. Notably, temporal patterning of dCA1 neural activity plays a crucial role in odorant working memory tasks^{11,17} and has been postulated to play a role in organizing memories¹⁰ raising the question whether it contributes to the neural mechanism for go-no go associative learning in this brain region. Hippocampal "time cells" store memory of the temporal order of events and signal changes in the temporal context^{10,11,18}. It has been hypothesized that the temporally structured activity of neurons make perceptually related responses coherent in time¹⁹, but it is unknown whether there is a time-tiled divergence of distinct patterns of neural activity elicited by each stimulus (stimulus divergence) in dCA1 that could contribute through sequential neural dynamics to behavioral responses reflecting decision-making in associative learning.

Using two-photon Ca²⁺ imaging, we evaluated ensemble decoding of stimuli from temporally patterned neural activity in dCA1 in mice engaged in an olfactory go-no go task where the animals receive a water reward after licking on a spout when presented with the S+ odorant and do not receive a water reward for the S- odorant²⁰ (Figure 1A). We characterized stimulus divergence of Ca²⁺ responses of individual cells (Regions of Interest (ROIs)); we decoded the identity of the stimulus from Ca²⁺ recording; and we determined whether the onset of divergence of stimulus responses takes place at different times after stimulus presentation, in a time-tiled manner.

RESULTS

96

97

98

94

95

Two-Photon Calcium Imaging in Dorsal CA1 in Head-Fixed Mice Undergoing a Go-

No Go Olfactory Associative Learning Task

99

100

101

102

103

104

105

106

107

108

109

110

111

112

113

114

115

116

Calcium imaging was performed through a GRIN lens in adult Thy1-GCaMP6f mice (n=4) expressing the Ca²⁺ indicator GCaMP6f in neurons in the SP in dCA1 (Figure 1A, Figure S1A). The majority of these GCaMP6f-expressing cells were expected to be pyramidal cells and did not co-localize with parvalbumin interneurons (Figure S1B). We refer to GCaMP6f-expressing cells as SP cells. In the go-no go experiments, head-fixed water-restricted mice initiated each trial by licking on the water spout. One of two odorants was delivered 1-1.5 seconds after the start of the trial and the odorant was presented for 4 seconds. Mice were trained to respond to S+ by licking at least once during two 2 second response windows (RWs) to obtain a water reward for reinforcement (Figure 1A). The water reward was not delivered when S- was presented and if mice licked during the two RWs for S- they experienced a delay penalty before the next trial start. Two-photon calcium imaging recordings were denoised²¹, motioncorrected²² and time-binned traces of nonnegative changes in fluorescence intensity $(\Delta F/F)$ were obtained for multiple ROIs using EXTRACT²³. Figures 1B,C,E and Video 1 show calcium imaging data in CA1 from a 20 minute session for a mouse proficient in the go-no go task (153 ROIs, proficient stage is percent correct >= 80%). The fluorescence traces displayed calcium transients whose timing was heterogeneous

when evaluated by the cross-correlation between the traces of all ROIs (Figure 1D). In this session a subset of the ROIs responded differentially during S+ vs. S- odorant trials (Figures 1C,E). These results suggest the existence of a complex time structure underlying the calcium responses from a population of dCA1 neurons in the go-no go task.

Mice Learn to Respond Differentially to the Rewarded and Unrewarded Odorants in the Go-No Go Task

In the first training session, the percent correct response to the odorants (S+: 1% heptanal, HEP, S-: mineral oil, MO) was between 45% and 65% correct for three of four mice (Figure S1 C-E, for the fourth mouse percent correct was 75% in the first session, Figure S1F). We classify the session as "learning stage" when percent correct behavior is between 45% and 65% correct. We then trained the mice in 3-6 training sessions per day. As shown in Figure S1 C-F the mice gradually reached the proficient stage. We recorded from a total of 19 learning stage sessions in three mice and 66 proficient sessions in four mice (Table 1). Once the mice had stable proficient performance the odorants were reversed (S+: mineral oil, MO, S-: 1% HEP) to investigate whether dCA1 calcium responses encode for the odorant's identity or valence. Percent correct behavior dropped immediately below 50% and gradually recovered to proficient (Figure S1C-F). We recorded from a total of 25 forward proficient stage sessions and 41 reversed proficient stage sessions in four mice. Finally, as discussed in the methods (Figure S2) odor delivery pinch valves emit a click sound at the start of the trial that

could be used to decode the stimulus. However, when the odorant is removed behavior drops to 50% (Figure S1 G-I) indicating that mice cue on odorants in this go-no go task.

142

143

144

140

141

Stimulus-divergent z∆F/F Responses are Heterogeneous and Divergence

Increases with Learning

145

146

147

148

149

150

151

152

153

154

155

156

157

158

159

160

161

162

The results shown in Figure 1C indicate that a subset of ROIs respond differentially to the two odorants. We proceeded to assess whether per ROI z-normalized $\Delta F/F$ ($z\Delta F/F$) time courses diverged between S+ vs. S- odorant trials. We compared the divergent zΔF/F time courses between S+ (Hit + Miss) and S- (CR + FA) trials, or we compared the $z\Delta F/F$ time courses for incorrect trials (Miss and FA) with correct trials (Hit and CR). In order to characterize the differential responses we classified z-normalized $\Delta F/F$ time course in S+ or S- trials within a session as divergent when the p-value for a generalized linear model (GLM) analysis of the difference between S+ and S- in the time span from -1 to 5.5 sec was below the p-value for significance corrected for multiple comparisons using false discovery rate²⁴. Figure 2A shows examples of single ROI divergent responses and Figure 2B shows a pseudocolor representation of the time courses for all ROIs diverging in z∆F/F between S+ and S- trials for the proficient stage. The time courses fall into two types as evidenced by hierarchical clustering (the cluster tree is shown on the left in Figure 2B) and by the cross correlogram of the per session z∆F/F time courses (Figure 2C). The first cluster, ROIs numbered 934 to1657 (red hierarchical branch), displays a decrease in z∆F/F for S+ and an increase for S- (Figure

2Fi). In contrast, the time course for cluster 2 (cyan hierarchical branch) shows an increase in $z\Delta F/F$ for S+ trials and a smaller increase for S- trials (Figure 2Fii).

Analysis of $z\Delta F/F$ divergent ROIs for the learning stage also displayed a similar heterogeneity in time courses (Figures S3B and S3C). The percent of divergent ROIs was not significantly different between learning and proficient stages (Figure 2Ei, t-test, p>0.05, 3 mice for learning, 4 mice for proficient). However, when the per cluster $z\Delta F/F$ (Figure 2G) was tested with GLM analysis there were statistically significant differences for S+ vs. S- and for learning vs. proficient for both clusters (p<0.05, number of observations, d.f. and F statistics are in Data S1A). These differences indicate that there are changes in $z\Delta F/F$ time course elicited by learning. Finally, the time course for error trials tended to be similar to the time course for correct trials (compare Hit vs. Miss and CR vs. FA in Figures 2H and I, p>0.05, Data S1A).

Stimulus-Divergent z∆F/F Responses Take Place at Discrete Times

Responses of a subset of CA1 pyramidal cells named odor-specific time cells take place at discrete time points in the delay period in a delayed non-match to sample task where the animals are presented sequentially with two odors¹¹. We asked whether we had similar time tiling for the onset of odorant divergence for $z\Delta F/F$ time courses. The time courses for $z\Delta F/F$ shown in pseudocolor in Figure 2B show visible differences in the times of the divergent responses (also see examples for individual ROIs in Figure 2A).

As shown in Figure 2D divergence times spanned the time period from trial onset to times after the reward was delivered.

187

188

189

185

186

Switching Rewarded to Unrewarded Stimulus Elicits Changes in z∆F/F Stimulus Responses Consistent with Response to the Valence of the Stimulus

190

191

192

193

194

195

196

197

198

199

200

201

202

203

204

205

206

207

In order to determine whether stimulus-divergent z∆F/F responses are divergent responses to the stimulus identity (e.g. odorant identity) vs. stimulus valence (are the stimuli rewarded?) we switched the rewarded S+ stimulus (1% heptanal, HEP) with the unrewarded S- stimulus (mineral oil, MO) after the animal became proficient. We define the original training condition (HEP as S+) as a "forward" go no go task, and then flipping the rewarded and unrewarded odors (MO as S+) as a "reversed" go no go task. This reversed go-no go task allows us to probe whether the divergent responses are responses to odor identity vs. odor valence. As shown in Figures S1C-F, percent correct behavior decreased below 50% after stimulus reversal. Subsequently, it recovered, reaching >80% indicating that the animal learned the new reversed valence of the stimulus. Figure 3A shows the z∆F/F time course for ROIs that responded with divergence to the stimuli when the animal was proficient in the forward task. We performed a cross-correlation analysis (Figure S4B) and we sorted the time courses into two clusters using a hierarchical binary cluster tree and computed average time courses for the two clusters (Figure 3Ci, Figure S4Ai). As in Figure 2, the responses to S+ (HEP) tended to be larger than responses to S- (MO) in the most abundant cluster of responses (cluster 2) in this forward task (Figure 3A).

Interestingly, in both the forward and reversed tasks the S+ elicited a larger $z\Delta F/F$ response for cluster 2 ROIs when the animal was proficient (Figure 3C). We quantified this shift in $z\Delta F/F$ time courses with reversal by determining the value for stimulus-induced changes in $z\Delta F/F$ in the window from 1 to 2 seconds. Figure 3D shows a bar graph of the changes in $z\Delta F/F$ for forward and reversed runs for cluster 2 (results for cluster 1 are depicted in Figure S4Aiii). When the $z\Delta F/F$ peak values were tested with GLM analysis there were statistically significant differences for both odorant and forward vs. reversed (p<0.001, Data S1B). These data suggest that most of the $z\Delta F/F$ stimulus responses are responses to the odorant valence.

For the mouse whose percent correct behavior is shown in Figure S1F we ran the last forward session and the two proficient reversed sessions on the same day allowing us to perform an analysis where the ROIs in the reversed sessions were matched to the ROIs in the forward session. Figure S4C shows divergent $z\Delta F/F$ time courses for matched ROIs in forward and reversed proficient sessions sorted into two clusters using a hierarchical binary cluster tree. Figure S4D shows the cross correlogram for these $z\Delta F/F$ time courses. In order to compare the forward and reversed divergence in $z\Delta F/F$ time courses we calculated d'^{25} per time point for $z\Delta F/F$ time courses for HEP vs. MO. A change in d' polarity indicates that the response is a response to the valence. The d' time courses for forward and reversed sessions for all divergent ROIs are shown in Figure S4E and Figure 3E plots the peak value of d' in the odorant period for the forward and reversed runs. Most of the d' values reverse polarity with the forward to

reversed switch indicating that these ROIs represent the odorant value. In conclusion, for proficient sessions (>80% correct behavior), most of the $z\Delta F/F$ divergent ROIs represent stimulus valence.

The Accuracy for Decoding Stimulus Increases with Learning and is Dependent on the Timing of the Training Window

We asked whether the information embedded within zΔF/F activity of all ROIs can be used to decode the stimulus (S+ vs. S-) using a GLM decoding algorithm. When we trained the GLM using a broad training time window spanning the odorant presentation period and the beginning of the reward period (0.5 to 5.5 sec) decoding accuracy started increasing above 0.5 slightly after trial start (~-1 sec) and reached ~0.8 through a window spanning the odorant period for the proficient animal (Figure 4Aii). In contrast, the decoding accuracy for the learning stage only reached ~0.65 (Figure 4Ai). The bar graph in Figure 4iii shows the accuracy for pre-odor (-1 to 0), odor (3.1 to 4.1) and reinforcement (4.5 to 5.5) trial periods. A GLM analysis yielded a statistically significant difference for odor and reinforcement time periods vs. pre-odor period and for the interaction between these trial period comparisons and proficient vs. learning stages (p<0.05-0.001), 279 observations, 270 d.f., 4 mice, GLM F-statistic=37.7, p<0.001 (Data S1C).

We then asked how the decoding accuracy time course varies depending on the training time window. As expected when the training window spanned a period before

stimulus presentation (-5 to -3 sec) accuracy did not increase above shuffled (Figure 4C, the p-value for GLM was >0.5 for all comparisons, see Data S1C). In contrast, when the training window spanned the reinforcement period (4.5 to 6.5 sec) decoding accuracy increased above 0.5 for the learning stage after the mouse was given the reinforcement (Figure 4Bi) and the increase in decoding accuracy above 0.5 shifted to the time when the odorant was presented when the mouse became proficient (Figure 4Bii). GLM analysis of the bar graph in Figure 4Biii indicated that these changes in decoding accuracy were statistically significant (p<0.001 for the interaction between odor period vs. pre-odor period and proficient vs. learning stages, 273 observations, 264 d.f., 4 mice, GLM F-statistic=45, p<0.001, Data S1C). Other decoding algorithms yielded similar results (Figure S5A, Data S1G). As expected the accuracy for stimulus prediction differs when different windows are used to train the GLM decoding algorithms.

Decoding of Decision Making in the Go-No Go Task from CA1 Neural Activity is

269 Time-tiled

Divergence of $z\Delta F/F$ responses between S+ and S- stimuli occurs at different times after trial start (Figures 2A and D, Figure S3A) suggesting that the onset of the increase in accuracy for stimulus decoding is time-tiled. In order to assess time tiling of the timing for decision making, we performed an analysis of the time course for accuracy of stimulus decoding from $z\Delta F/F$ responses of subsets of ROIs per session for proficient

mice. The number of ROIs used to calculate GLM decoding per session was varied

from 1, 2, 5 and 15 ROIs to all ROIs per session. For this decoding analysis we trained the GLM algorithm with $z\Delta F/F$ data in the broad training time window (0.5 to 5.5 sec, Figure 4A).

Figure 5A shows histograms of decoding accuracy calculated in the odor period (3.1 to 4.1 sec) for stimulus decoding performed with zΔF/F from these subsets of limited numbers of ROIs (blue bars) (also see examples in Figure S6A-C). For comparison we also show a histogram for accuracy values calculated after shuffling the odorant contextual identity (brown bars). As the number of ROIs per decoding run decreases, stimulus decoding accuracy declines (compare Figure 5Av with 5Ai). In addition, the pre-odor accuracies also decrease as the number of ROIs per decoding run is decreased (compare Figure 5Bv with 5Bi). A GLM analysis yields significant differences in decoding accuracy for comparisons between the number of ROIs per decoding run and the time periods, p<0.001, 4 mice, 27344 observations, 27344 d.f., F-statistic 798, p-value <0.001 (Data S1D).

We quantified the divergence time, calculated when accuracy increased above 0.55 after trial start for at least 0.2 sec, for decoding accuracy time courses with odor period decoding accuracy >0.65 (Figure S6E). Histograms of divergence times calculated for the different multiple ROI decoding runs are shown in Figure 5C. The divergence times decrease as the number of ROIs used for decoding calculation increases (compare Figure 5Ci with Figure 5Cv). A GLM analysis of divergence times yields significant differences for comparisons between accuracies calculated with different numbers of

ROIs, p<0.001, 4 mice, 27354 observations, 27349 d.f., F-statistic 1400, p-value <0.001 (Data S1D). This analysis indicated that the onset of the increase in stimulus decoding accuracy is time tiled.

Finally, we generated a pseudocolor plot of the time course of decoding accuracy to better illustrate the time tiling of accuracy onsets (Figure 5D). When decoding from individual ROIs there is a large variance in the start of the increase in accuracy ranging from trial start to reward delivery (Figure 5Di). Computing average accuracy time courses for different divergence time periods shows that the onset of the increase in decoding accuracy is time-tiled and that decoding accuracy calculated for the earliest divergence time period is biphasic with a small increase at trial start followed by a larger increase after odor onset (Figure 5Dii). In contrast, when decoding accuracy is computed with all ROIs per session there is less variance in the time for onset of the increase in decoding (Figure 5Diii and 5Div). These data show that the onset of increases in decoding accuracy, predicting time of decision making, is time-tiled in hippocampal CA1 suggesting that these are decision-predicting time cells.

Lick Decoding and Stimulus Decoding Differ in their Relationship to Lick Behavior

Next we asked how stimulus decoding prediction is related to lick behavior (quantified as lick fraction defined as the fraction of trials when the animal was making contact with the lick tube). In addition, we asked whether it was possible to decode lick behavior

from neural activity and whether the relationship between lick prediction and lick fraction differed from the relationship between stimulus prediction and lick fraction. We performed this analysis separately for correct responses (Hits and CRs) and incorrect responses (Miss and FAs)(Figure 1A).

There was a transient increase in lick fraction for all trial types when the animal started the trial by licking on the water spout (arrow in Figure 6A). For Hits (red) this transient increase was followed by a steady increase in lick fraction during the odor period (0-4 sec), while for CR trials (blue) there was a decrease toward zero shortly after odorant presentation. In contrast, for Miss trials, the lick fraction did not increase during the first second of the odorant period (cyan), and for FA trials, the lick fraction was high for the first half of the odorant period (magenta). Figure 6B is a bar graph showing the mean lick fraction during the first and second 2 sec response windows (RWs) during the odorant period (RWs are defined in Figure 1A). A GLM analysis yields significant differences in mean lick fraction for comparisons between CR or Miss vs. FA or Hit and for the interaction of Miss or Hit and FA and the RWs, p<0.001, 4 mice, 452 observations, 441 d.f., F-statistic 36.7, p-value <0.001 (Data S1E).

The accuracy for neural network decoding of lick fraction from $z\Delta F/F$ for all ROIs per session when the mice were proficient (four mice, 66 sessions) is shown in Figure S5B. In contrast with accuracy for stimulus decoding that starts diverging from shuffled at the trial start (Figure 4Aii) lick decoding accuracy starts diverging from shuffled after the odorant presentation (Figure S5B). The bar graph in Figure S5C shows the mean lick

decoding accuracy data for pre-odor (-1 to 0), odor (3.1 to 4.1) and reinforcement (4.5 to 5.5) time periods. A GLM analysis yielded a statistically significant difference for odor and reinforcement time periods vs. pre-odor period and for the interaction between these time period comparisons and shuffling (p<0.001), 378 observations, 369 d.f., 4 mice, GLM F-statistic=62.1, p<0.001 (Data S1G). Figures 6C and D show the lick prediction time course and mean lick prediction calculated in the RA windows for the different trial types. A GLM analysis yields significant differences in mean lick prediction for comparisons between Hit or Miss and FA and for the interaction of Hit and FA and the RWs, p<0.001, 4 mice, 488 observations, 477 d.f., F-statistic 24.3, p-value <0.001 (Data S1E).

Figure 6E shows the time course for stimulus prediction. For Hits (red) there was a steady increase in stimulus prediction that started at trial onset and leveled to a value of ~0.8 during the odor period for Hits (red) while for CR trials (blue) there was an initial increase after trial start that decreased to ~0.2 during the odor period. For Miss trials stimulus prediction appeared to increase to a value below Hit prediction (cyan). For FA trials stimulus prediction started increasing at the trial start, but did not decrease to ~0.3 during the odor period (magenta). Figure 6F is a bar graph showing the mean stimulus prediction during the first and second 2 sec response windows (RWs) during the odorant period. A GLM analysis yields significant differences in mean stimulus prediction for comparisons between CR, Miss or Hit, and FA, p<0.05, 4 mice, 452 observations, 441 d.f., F-statistic 57.3, p-value <0.001 (Data S1E).

The time course for lick fraction (Figure 6A) appears to be similar to the time course for lick prediction (Figure 6C) and appears to differ from stimulus prediction (Figure 6E). Indeed, the relationship between lick fraction and lick prediction was linear (Figure 6G). In contrast, the relationship between lick fraction and stimulus prediction differed between S+ (Hit/Miss) and S- (CR/FA) (Figure 6H). For Hits and Miss the stimulus/lick fraction relationship was linear (Figure 6H, cyan and red circles), while for CR/FA points (Figure 6H, magenta and blue circles), the relationship appeared to be quadratic and the points did not fall along the Hit/Miss line. Therefore, the relationship between lick fraction and stimulus prediction in CA1 does not follow the simple linear relationship that is expected from neural activity closely related to motor action. Instead, the relationship differs strikingly for S+ vs. S- stimuli. However, decoding lick behavior from the same neural activity did yield a prediction that showed a linear relationship with lick fraction.

Stimulus Decoding Between Trials is Biased to Predict the Unrewarded Stimulus and there are Sudden Brief Shifts to Rewarded Stimulus Prediction

We proceeded to explore whether decoding of stimulus contextual identity from neuronal activity in CA1 between trials predicted one of the two stimuli for proficient mice engaged in the go-no go task. Figure 7A shows a time course for predicting the stimuli by GLM decoding calculated during an imaging session. As in Figure 4A, GLM was fit to neural activity for all ROIs during the 0.5 to 5.5 sec spanning most of the odorant window. A prediction value of 1 corresponds to S+ prediction and a value of 0 represents S-. The blue shade shows the 5th to 95th percentile band for prediction

calculated after shuffling the stimulus labels. Trials are bounded from start to end of odor epoch by vertical lines (cyan: S+, magenta: S-). As expected, within trials prediction increases to 1 for some time longer than the odorant window during S+ trials while it increases briefly at the start of S- trials but returns to zero before the end of the odorant period. Figure 7B shows the within trial mean prediction time course for all trials in proficient sessions for the 4 mice (a total of 1848 trials in 66 sessions). For this withintrial decoding the prediction starts increasing before trial start for both the S+ and S- trials and it diverges between S+ and S- at the start of the trial. The bar graph in Figure 7C shows the S+ and S- prediction for a baseline period (-2.5 to -1.5) and an odor period (2 to 4.1 sec). A GLM analysis yields significant differences for baseline vs. odor time periods and for the interaction between S+ vs. S- and time periods, p<0.001, 4 mice, 220 observations, 213 d.f., F-statistic 194, p <0.001 (Data S1F). Thus, within the trial stimulus prediction starts increasing at trial onset and diverges between rewarded and unrewarded odorant trials shortly after trial onset.

Intriguingly, the average prediction calculated between trials is lower than shuffled (Figures 7A and 7D) indicating that the default decoding is S- for most of the time between trials (GLM p-value for between vs. shuffled <0.001, 110 observations, 105 d.f., F-statistic 70.7, p<0.001, Data S1F). However, there are precise brief shifts of prediction to 1 (arrow in Figure 7A). We identified these spontaneous shifts of prediction to 1 between trials by finding increases beyond the 95 percentile of the shuffled prediction values (blue shade in Figure 7A). We found a total number of 1635 spontaneous shifts to S+ prediction between trials in 66 sessions. The duration of these

spontaneous shifts varied between a fraction of a second to two seconds. The cyan bounded line in Figure 7F shows the mean time course for between trial spontaneous shifts compared to an adjacent between trials time period with no spontaneous changes in prediction ("no change", magenta). The bar graph in Figure 7G shows a significant difference between the prediction before the onset of the spontaneous increase in prediction and the peak of prediction for the spontaneous shift. A GLM analysis yields significant differences for spontaneous shift in prediction vs. no shift and for the interaction between spontaneous vs. no shift and baseline vs. peak time windows, p<0.001, 4 mice, 192 observations, 185 d.f., F-statistic 703, p <0.001 (Data S1F).

The fact that there is a spontaneous shift in stimulus prediction from S- to S+ between trials raises the question whether the neural activity at the time of spontaneous prediction shifts is more correlated to the activity during rewarded odorant trials as opposed to unrewarded odorant trials. We calculated per session the correlation between $z\Delta F/F$ values for all ROIs at the onset of the spontaneous shift to S+ between trials and $z\Delta F/F$ values for all ROIs at each time point during the the time course of either S+ or S- trials. Figure 7E shows the time courses for these correlations averaged over all ROIs. The correlation of spontaneous $z\Delta F/F$ with S+ diverges from the correlation with S- shortly after the start of the trial and remains high for a few seconds after the reward. A GLM analysis yielded significant differences in average correlations for comparison of the time windows (baseline vs. odor) and for the interaction between S+ vs. S- and time window, p<0.001, 4 mice, 216 observations, 209 d.f., F-statistic 15.7,

p-value <0.001 (Data S1F). This indicates that neural activity at the onset of the spontaneous shift resembles neural activity during rewarded trials.

Finally, we asked whether lick behavior differed between spontaneous prediction shifts compared to no change. The blue bounded line in Figure 7H shows the lick fraction during spontaneous shifts and the magenta bounded line shows the lick fraction during an adjacent between trial time period with no spontaneous changes in prediction ("no change"). We found that the lick fraction is slightly higher during the prediction shifts compared to no change (Figure 7H). The bar graph in Figure 7I shows the lick fraction calculated 2 seconds before and 2 seconds after the shift. A GLM analysis yields significant differences in lick fraction for comparison between spontaneous prediction shift and no change, p<0.001, 4 mice, 192 observations, 185 d.f., F-statistic 28.3, p-value <0.001 (Data S1F). This indicates there is a tendency for slightly elevated licking in between trial epochs where a spontaneous shift occurs.

DISCUSSION

In this study we performed two photon imaging of calcium responses in head-fixed mice engaged in an associative learning go-no go task where they decide whether they lick to obtain a reward when presented with rewarded (S+) or unrewarded (S-) odorants.

Unlike other sensory systems, the efferent axons from the olfactory bulb bypass the thalamus and synapse (directly or through relay in the piriform cortex) onto the LEC

constituting a primary sensory input to dCA1^{26,27}. Olfactory responses mediated by LEC input are particularly prominent in the mouse dCA1²⁸⁻³⁰, and odorant responses in dCA1 are known to be involved in tasks such as delayed match/non-match to sample (working memory)^{11,17}, odor place associative learning²⁸, odorant gradient navigation³¹ and odorant sequence evaluation³².

Dorsal CA1 is arguably one of the most studied areas of the brain involved in learning and memory³³⁻³⁶ and it is well documented to play a role in spatial and episodic learning and memory^{10,12}. Yet, its role in go-no go associative learning has been called into question. Li et al. found that calbindin positive pyramidal neurons in CA1 became more selective for odorants as animals became proficient in the go-no go task and optogenetic inhibition of these cells slowed learning¹⁶. In contrast, a study by Biane and co-workers found that the accuracy of odor decoding in dCA1 was not altered by learning in the go-no go task¹⁵. Here we find that learning results in increased stimulus divergence of zΔF/F responses for single SP cells (Figure 2); and that there is a substantial increase in stimulus decoding accuracy calculated from the SP cell ensemble when the animal becomes proficient in the go-no go task (Figure 4). Our results are consistent with a role for dCA1 pyramidal cells in go-no go associative learning proposed by Li et al. and with local field potential (LFP) power in dCA1^{37,38} upon learning in dCA1 in the go-no go associative learning task.

For proficient mice, prediction for stimulus decoding tends to represent the correct stimulus even when the animal makes a mistake (Figures 2H, 6E and 6H). In contrast,

for lick decoding the predictions for errors align closer with the mistakes the animal makes in the lick response (Figure 6G). One explanation for this may be that although the animal does perceive the odorant, it is satiated and therefore chooses to make a mistake (not licking) on purpose. These results suggest that CA1 encodes for different information manifolds that can be used differentially depending on the context and behavioral purpose. Whether this is the case needs to be evaluated in future studies.

We asked whether dCA1 SP cells represent the odorant identity or its valence. We found that predicting the stimulus decoded from z∆F/F ensemble neural activity in dCA1 was biased towards S- between trials (Figures 7A and D). This is unlike stimulus identity decoding in areas such as the auditory cortex, where there is no bias in stimulus prediction³⁹ suggesting that dCA1 ensemble activity represents stimulus value as opposed to odorant identity. Indeed, when the stimuli were reversed the responses were consistent with representation of valence for a large portion of the ROIs (Figure 3E). This result is consistent with valence representation found in olfactory bulb single units after reversal in the go-no go learning task^{40,41}, functional plasticity of sensory inputs elicited by learning in the olfactory bulb^{42,43}, and with decoding of stimulus contextual identity after stimulus reversal for measurements LFP power in dCA1³⁸. In addition, the shift we find in dCA1 neural odorant representation upon reversal of reward is reminiscent of remapping of hippocampal space cells in different contexts that can be explained by associative learning⁴.

Time-tiled odorant responses by "time-cells" in dCA1 are thought to be involved in delayed match/non-match to sample where they presumably provide short term working memory of the identity of the first odorant that is presented in the task^{11,17}. Interestingly, we find that for the go-no go task the divergence between S+ and S- stimuli in z∆F/F odorant responses of individual SP cells takes place at different times between trial start and reinforcement (Figure 2D) and, consistent with these results, stimulus decoding accuracy decoded from single neuron activity starts diverging from accuracy computed from shuffled stimulus labels (50%) at discrete times ranging from trial start to several seconds after reinforcement (Figures 5Di and S6). Therefore, decision making for the difference between stimuli based on single cell dCA1 neural activity takes place at different discrete times in dCA1. This finding of "decision-making prediction time-cells" is novel and complementary to stimulus time-cells engaged in delayed match/non-match to sample tasks^{11,17}. We hypothesize that this discrete time tiling of information for decision making in dCA1 by sequential neural dynamics plays a role in go-no go associative learning by representing a memory of whether the rewarded odorant is presented that the mouse uses to decide whether it should sustain licking to get a reward. As recently proposed for spatial navigation³⁶, neuromodulatory inputs may sculpt hippocampal representations to either provide stimulus valence information or shift the distribution of states, 'weighting' rewarded stimuli more heavily than unrewarded stimuli. Whether this is the case will be determined in future studies.

525

526

527

505

506

507

508

509

510

511

512

513

514

515

516

517

518

519

520

521

522

523

524

Finally, our data raise the question of the specific role of sequential activity in associative learning in dCA1. On one hand, sequential activity in dCA1 is often

associated with transition in the state space where each state encodes for a predictive representation of future states given the current state^{44,45}. Under this interpretation, time-tiling represents state transition in a cognitive map representing the temporal task structure. On the other hand, sequential activity potentially encodes a single working memory that makes the animal more likely to choose a specific outcome as time passes. Previous modeling work revealed that depending on the model configuration, a recurrent neural network learns to represent working memory either by sequential or persistent activity⁴⁶. It indicates that time-tiling might encode a binary decision (go or nogo) with spatial-temporal patterns. Sequential working memory representation is also beneficial for binding multiple information, such as stimulus identity, valence, and context, into a single working memory^{47,48}. Future work will clarify whether time-tiling in the decision period represents a transition in the cognitive map or a go/no-go decision variable.

542 **ACKNOWLEDGEMENTS** 543 544 We would like to thank Brooke Baxter for technical assistance. This research was 545 supported by the US National Institutes of Health (NIH UF1 NS116241 and NIH R01 546 DC000566), and the National Science Foundation (NSF BCS-1926676). 547 **CONTRIBUTIONS** 548 549 M.M., F.S.de S., E.G. and D.R. conceived and designed the experiments, F.S.de S. 550 performed the surgeries, acquired experimental data and did data analysis, M.M. 551 performed experiments and data analysis, E.G. and G.F. designed and implemented 552 optical instrumentation, G.F. provided technical assistance with multiphoton microscopy, 553 S.A. and D. T. performed sound recordings and analysis, J.R. assisted with immunohistochemistry, A.G.-P. provided technical help, generated illustrations and did 554 555 immunohistochemistry, J.P. generated code for NWB data sharing, K.S. provided 556 advice in experimental design and analysis and writing, N.H. provided advice on data analysis and writing, M.M., F.S.de S. and D.R. wrote the manuscript and all authors 557

560 **DECLARATION OF INTERESTS**

edited the manuscript.

The authors declare no competing interests

563

558

559

561

STAR * METHODS

565 Key resources table

| REAGENT or RESOURCE | SOURCE | IDENTIFIER |
|---|--|--|
| Antibodies | , | |
| Donkey anti-rabbit Alexa Fluor 594 secondary antibody | Jackson Immunoresearch | 11-585-152 |
| Donkey anti-mouse secondary antibody Alexa Fluor 647 | Jackson Immunoresearch | 715-606-150 |
| Mouse anti-PV primary antibody | Sigma-Aldrich | P-3088 |
| Rabbit anti GFAP antibody | Abcam | ab7260 |
| Deposited data | | |
| Raw and analyzed data | Mendeley data | doi: 10.17632/7gn6dj89t3.1 |
| Experimental Models: Organisms/Strains | · | |
| Thy1-GCaMP6f mouse, C57BL/6J-Tg(Thy1-GCaMP6f)GP5.17Dkim/J | The Jackson Laboratory | 025393 |
| Software AND Algorithms | | |
| Matlab 2022b and 2023a | https://www.mathworks.c om/products/matlab.html | N/A |
| Code to generate the main figures | https://github.com/restrep d/CA1_Figures | N/A |
| Data to generate the main figures | Mendeley data doi: 10.17632/7gn6dj89t3.1 | Please note that this is a temporary doi that will be replaced by a permanent doi once repository is published |
| Other | · | |
| GRIN lenses | GRINTECH GmbH | NEM-050-25-10-860- DS |
| Metabond | Thermo Fisher | NC0877382, NC2048900, NC2048904 |
| Paraformaldehyde | Electron Microscopy Sciences | 15714-S |
| DAPI | Thermo Fisher | 62248 |
| Buprenorphine SR/ER | Zoopharm/Wedgewood | |
| Vetbond | MWI | 006245 |
| Light mineral oil | Fisher | O121-1 |
| Heptanal | Sigma-Aldrich | H-6129 |
| OCT | Sakura Finetech | 4583 |

| 567 | Data S1. Statistical analysis. Related to STAR Methods and Figures 1 to 7 |
|-----|--|
| 568 | A) GLM statistics for the $z\Delta F/F$ bar graphs in Figures 2G and I |
| 569 | B) GLM statistics for the z∆F/F bar graphs in Figures 3D and Figure S4Aiii |
| 570 | C) GLM statistics for the accuracy bar graphs in Figure 4 |
| 571 | D) GLM statistics for Figure 5 |
| 572 | E) GLM statistics for Figure 6 |
| 573 | F) GLM statistics for Figure 7 |
| 574 | G) GLM statistics for Figure S5 |
| 575 | |
| 576 | RESOURCE AVAILABILITY |
| 577 | |
| 578 | Lead contact |
| 579 | Further information and requests for data should be directed to and will be fulfilled by |
| 580 | the lead contact, Diego Restrepo (diego.restrepo@cuanschutz.edu). |
| 581 | |
| 582 | Materials availability |
| 583 | This study did not generate new unique materials. |
| 584 | |
| 585 | Data and code availability |
| 586 | The source data to reproduce the figures are available at Mendeley Data (doi: |
| 587 | 10.17632/7gn6dj89t3.1). Please note that this is a temporary doi that will be |
| 588 | replaced by a permanent link and doi once the repository is published |
| | |

Analysis code has been deposited at GitHub
 (https://github.com/restrepd/CA1_Figures).

591

592

 Any additional information required to reanalyze the data reported in this paper is available from the lead contact upon request.

METHOD DETAILS

Animals

All experimental protocols were approved by the Institutional Animal Care and Use Committee of the University of Colorado Anschutz Medical Campus, in accordance to NIH guidelines. Mice were bred in the animal facility, and we used both males and females, a total of four adult Thy1-GCaMP6f mouse (Jax 025393 C57BL/6J-Tg(Thy1-GCaMP6f)GP5.17Dkim/J) for head-fixed awake behaving two-photon imaging of CA1 pyramidal cells through a GRIN lens. We used the 5.17 strain of Thy1-GCaMP6f mice because of their strong expression of GCaMP6f in CA1⁴⁹. The animals were housed in a vivarium with a 14/10 h light/dark cycle. Food was available ad libitum. Access to water was restricted in behavioral training session according to protocols. All mice were weighed daily and received sufficient water during behavioral sessions to maintain >80% of their original body weight.

Surgical Procedures

Mice were injected with carprofen (5 mg/kg, IP) one hour before surgery and were anesthetized with ketamine/xylazine (IP, 100 mg/kg and 10 mg/kg, respectively). Anesthetic redosing was assessed by pinching the hind feet every 5 min. A craniotomy of diameter ~1.2 mm was made over the right hippocampus and a GRIN lens of 4 mm length and 1 mm diameter (GRINTECH, NEM-050-25-10-860-DS) was implanted at 1.8 mm lateral and 2.4 mm caudal of Bregma and 1.25 mm below dura ³¹. The GRIN lens edges were sealed with Vetbond glue (3M, USA) and a custom-made steel head bracket was glued to the skull with Metabond (Parker, USA) for head-fixing and

imaging. The mice were treated with buprenorphine SR/ER for two days after surgery (0.05 mg/kg, SQ). dCA1 imaging was initiated two weeks after surgery.

Immunohistochemistry and CT-Scan

Immunohistochemistry was performed for Figure S1A after animals finished all the training to visualize GCaMP6f expression in the hippocampus CA1 region and the track of the GRIN lens implant. Immunohistochemistry for Figure S1B was performed on an adult mouse that had not been trained. Mice were sacrificed and transcardially perfused with ice cold 4% paraformaldehyde (PFA), followed by equilibration in 30% sucrose. After the brain sank, the tissue was embedded in optimal cutting temperature (OCT) compound and was frozen at -80°C. Slices of 60 µm thickness were cut with a Leica cryostat. For Figure S1A the slices were stained with rabbit anti-GFAP primary antibody (Ab7260, Abcam, USA) and Alexa Fluor 594 donkey anti-rabbit secondary antibody (11-585-152, Jackson Immunoresearch, USA).

For Figure S1B the slices were stained with mouse anti-parvalbumin (anti-PV) primary antibody (Sigma-Aldrich P-3088) and Alexa Fluor 647 donkey anti-mouse secondary antibody (715-606-150, Jackson Immunoresearch, USA). The slices were counterstained with DAPI (Thermo Fisher Scientific, USA) and imaged using a confocal laser scanning microscope (Nikon A1R, Japan). We find that GCaMP6f expression does not overlap with PV expression in dCA1 in Thy1-GCaMP6f mice (Figure S1B) indicating that the SP cells we imaged are not PV interneurons. However, it is possible that a subset of the SP divergent cells are interneurons. Future studies will be necessary to

study the involvement of dCA1 interneurons in responses during in mice engaged in the go-no go task.

To further verify the 3D position of the GRIN lens in the skull and brain, we performed microCT-Scan recording. We perfused the mice with PBS and the ex-vivo PFA fixed head was used for acquiring the microCT imaging on a Siemens Inveon microCT system (Siemens, Germany).

Go-No Go training

Mice were water deprived by restricting daily water consumption to 1-1.5 ml. Mice were monitored for signs of dehydration or decreased body weight below 80% of the initial weight. If either condition occurred, the animals received water ad-lib until they recovered. When the animals were water-deprived, they were trained in a head-fixed olfactory go-no go task with 1% HEP vs MO odorant application (Sigma-Aldrich, USA)^{20,41,50}. An olfactometer controlled valves to deliver a 1:40 dilution of odorant at a rate of 2 L min⁻¹. An Intan RHD2000 acquisition system (Intan, USA) recorded licks measured by monitoring the resistance between the lick spout and the floor of the olfactometer. The water-deprived mice started the trial by licking on the water port. The odorant was delivered after a random time interval ranging from 1 to 1.5 seconds. In S+ trials, the mice needed to lick at least once in two 2 sec lick segments to obtain a reward (0.1 g ml⁻¹ sucrose water) (Figure 1A). In S- trials, the mice need to refrain from licking in one of the two 2 sec segments to avoid a longer inter-trial interval (+ 10 sec). The animal's behavior performance was evaluated in a sliding window of 20 trials and

the calculated value was assigned to the last trial in the window. Therefore, it estimated the performance in the last 20 trials. The percent correct value represents the percent of trials in which the animal successfully performed appropriate actions (100*(Hits+CRs)/number of trials), and we considered the animal proficient if the percent correct performance was above 80%. In reverse go-no go training sessions the S+ and S- odorants were switched after reaching a proficient level in forward training.

Acoustic recordings of auditory cues at the start of the trial in the go-no go task

In addition to the odorant cue the olfactometer emits a click at the start of the trial when one of the two odorant valves opens 1-1.5 sec before odorant onset. Acoustic recordings of the olfactometer were made using a GRAS 46BH-1 omnidirectional microphone and GRAS 26AC-1 preamplifier with Type 12AA power module, M-Audio Pro interface, and Audacity software. The microphone was positioned to approximate the location of the mouse's head during experiments. Recordings were time-aligned to experimental hardware using a trigger pulse. Recordings were windowed 7 seconds prior to 15 seconds following stimulus offset and separated according to S- or S+ conditions in MATLAB. Spectrograms of each stimulus were then generated to identify auditory events.

Figures S2B-C show a sound spectrogram of the click recorded with the ultrasound microphone at the location of the mouse's head in the two-photon microscope aligned with the opening of the odorant valve. Figure S2D shows that the identity of the odorant

valve (S+ vs S-) can be decoded from the sound click using a generalized linear model (GLM) decoding algorithm, albeit with low accuracy (~ 0.65) (ranksum test p<0.05, 58 trials for decoding stimuli vs. 290 trials for shuffled stimulus decoding).

While this task provides both olfactory and sound sensory inputs, the mouse cues on the olfactory stimulus as shown by the fact that percent correct behavior decreases close to 50% when the odor cues are removed while the valve opening (and consequent sound) are not altered (Figure S1G-I, consistent with previous studies with the same olfactometer⁵¹).

Two-photon imaging of dorsal hippocampus CA1 activity in animals undergoing the Go-No Go task

All the animals were first habituated to the setup to minimize stress during the imaging experiments. All the imaging sessions started at least 10 minutes after the mice had been head-fixed. The head fixed two-photon imaging system consisted of a movable objective microscope (MOM, Sutter Instrument Company, USA) paired with a 80 MHz, ~100 femtosecond laser (Mai-Tai HP DeepSee, Spectra Physics, USA) centered at 920 nm. The MOM was fitted with a single photon epifluorescence eGFP filter path (475 nm excitation/500-550 nm emission) used for initial field targeting followed by switching to the two-photon laser scanning path for imaging GCaMP6f at the depth of the CA1 cell body layer. Either the galvometric laser scanning system or a resonant scanner was driven by SlideBook 6.0 (Intelligent Imaging Innovations, USA). The two-photon time lapses were acquired at 395 x 380 pixels using a 0.4 NA/10x air objective (Olympus,

Japan) at either 5.3 Hz (galvo) or 20 Hz (resonant). On the day of initial imaging, a FOV was selected to image a large number of active hippocampal CA1 neurons through the GRIN lens, and GCaMP6f movies for several sessions (12-40 trials each) were collected each day. After two-photon imaging a second image of the vasculature was captured with wide field epifluorescence to reconfirm the field.

Statistical analysis

Statistical analysis was performed in Matlab R2022b or R2023a (Mathworks, USA). Statistical significance for changes in measured parameters for multiple factors such as learning and odorant identity (S+ vs. S-) was estimated using a generalized linear model (GLM)⁵² with post-hoc comparisons performed either with a two-sided t test, or a ranksum test, depending on the result of an Anderson-Darling test of normality. Post-hoc tests were corrected for multiple comparisons using the false discovery rate p-value (pFDR)²⁴. Asterisks in bar graphs specify statistically significant differences (p<pFDR) on post-hoc tests. Not all statistically significant differences are shown with asterisks because showing all significant differences would make the figures too complicated. However, all pairwise post-hoc test p-values and pFDR are shown in Data S1. Finally, we provide 95% confidence intervals (CIs)⁵³ estimated by bootstrap analysis of the mean by sampling with replacement 1000 times using the bootci function in MATLAB (shown in the figures as vertical black lines for bar graphs or shade bounding of mean value lines for time courses).

Data analysis

731

732

733

734

735

736

737

738

739

740

741

742

743

744

745

746

747

748

749

750

Raw imaging data was first surveyed in ImageJ 1.52 (NIH, USA) to exclude image sequences exhibiting axial movement. We did not find evidence of axial movement while the animal was engaged in the go-no go task. The raw imaging data was processed with DeepCAD-RT to denoise time-lapse images (https://github.com/cabooster/DeepCAD-RT)²¹, and then motion corrected with NoRMCorre algorithm²². The nonegative fluorescence traces were generated with EXTRACT (https://github.com/schnitzer-lab/EXTRACT-public)²³ with appropriate parameters. After Extract analysis, the $\Delta F/F$ traces of the spatial components were sorted and we assigned trial traces to different behavioral events (S+: Hit and Miss, S-: CR and FA) and aligned them to trial start, odorant onset or reinforcement delivery for further analysis. We chose to use the nonegative $\Delta F/F$ transients to perform the data analysis. These $\Delta F/F$ transients contain information on firing rate because calcium is a leaky integral of spikes. This resulted in reliable assessment of decoding of contextual odorant identity and lick behavior. However, a limitation of this analysis is that it may miss information encoded by neuronal firing. Because calcium imaging represents a leaky integral of neuronal firing the onset of the response is well represented, the end of the neuronal response is not. The data were converted into the NWB format (https://doi.org/10.1101/2021.03.13.435173) and organized into a BIDS-like (https://doi.org/10.1038/sdata.2016.44) structure.

751

752

753

Data analysis was performed using custom code in Matlab R2022b or R2023a. Mice were trained in 3-6 training sessions per day. Analysis was performed per session and

classified into either the learning stage with percent correct behavior within the 45-65% range (blue in Figure S1C-I) or the proficient stage with percent correct behavior in the 80-100% range (red in Figure S1C-I). The number of ROIs per session and the number of learning and proficient sessions used for the analysis in the different figures is shown in Table 1. For each ROI we z-scored Δ F/F by dividing by the standard deviation of Δ F/F calculated over the entire session (we call this z scored Δ F/F, z Δ F/F). Below we describe the different data analysis methods.

Divergent cell detection and analysis

Whether a cell's $z\Delta F/F$ diverged between S+ and S- (Figures 2 and 3) was determined as follows: Only sessions with a minimum of 12 trials were included. For the rest of the ROIs the $z\Delta F/F$ in the session was considered to be divergent if the GLM p-value for S+ vs. S- in the time span from -1 to 5.5 sec was below the pFDR. Examples of the time course $z\Delta F/F$ for divergent ROIs are shown in Figures 2A and S3A.

As shown in Figures 2B, 3A and 3B, the per trial time courses for $z\Delta F/F$ were heterogeneous. In order to quantify the heterogeneity we calculated within-trial cross-correlation coefficients between all divergent $z\Delta F/F$ time courses (including both S+ and S- in the calculation) for all divergent ROIs (e.g. Figure 2C). The $z\Delta F/F$ time courses for the different ROIs were then separated into different clusters by estimating an agglomerative hierarchical cluster tree using the linkage function of MATLAB. The number of clusters was specified arbitrarily.

In order to quantify the divergence in z∆F/F between HEP and MO trials for Figure S4 we calculated d', which is a measure of the difference in between two distributions.

780
$$d' = \frac{\text{mean}(z\Delta F/F(\text{HEP})) - \text{mean}(z\Delta F/F(\text{MO}))}{\sqrt{(SD(z\Delta F/F(\text{HEP}))^2 + SD(z\Delta F/F(\text{MO}))^2)/2}}$$
(2)

where SD is the standard deviation. As done for $z\Delta F/F$ time courses we used cross-correlation coefficients and an agglomerative hierarchical cluster tree to sort the time courses shown for d' in Figure S4E,F.

Stimulus decoding

Stimulus decoding was performed using GLM (fitglm in MATLAB). The algorithm was trained per session for all time points and all trials within time periods and number of ROIs per session was indicated in the text. Only sessions with 16 or more trials were processed. The predicted stimulus was assessed using leave one trial out, and winner takes all procedures. We report the results of GLM decoding, but we obtained similar results with linear discriminant analysis, neural network decoding, binary decision tree decoding and support vector machine decoding (Figure S5A).

Stimulus decoding with subset of ROIs

For GLM stimulus decoding performed with a subset of 1, 2, 5 or 15 ROIs (Figure 5) decoding was performed in separate runs with 40 unique subsets of ROIs drawn randomly from the total number of ROIs per session.

For decoding with small numbers of ROIs accuracy fell below 0.5. The reason was that for some of these decoding runs the majority of S+ and S- z∆F/F values were zero with one or two trials with a non-zero z∆F/F value. This is illustrated in Figure S6 where we show several examples of stimulus decoding accuracy when the decoding was performed with z∆F/F responses of individual ROIs. We found that for a subset of single ROIs decoding accuracy started increasing at different times after the trial started and reached accuracy values above 0.65. Three examples of decoding accuracy time courses and their corresponding z∆F/F time courses for S+ and S- trials are shown in Figure S6A-C. In Figure S6A, accuracy increases to ~0.6 at the start of the trial (immediately following valve click and before odorant addition) and increases to a higher value (~0.8) after odorant presentation. In Figures S6B and C, there is no increase in accuracy at the start of the trial and accuracy increases either shortly after odorant addition (Figure S6B) or ~3 sec after odorant addition (Figure S6C). A histogram of average z∆F/F values per trial computed during the odor period (3.1 to 4.1 sec) showed a clear difference between S+ and S- trial $z\Delta F/F$ for these three examples (Figures S6A-Ciii). In addition, we found a subset of individual ROIs whose decoding yielded decreases in accuracy below 0.5. An example is shown in Figure S6D, where the accuracy decreased to ~0.1. These decreases in accuracy took place for ROIs with largely overlapping S+ and S- odorant period $z\Delta F/F$ values except for one or two trials where the z\Delta F/F deviated from the other trials as evidenced in the histogram in Figure S6Diii.

821

800

801

802

803

804

805

806

807

808

809

810

811

812

813

814

815

816

817

818

819

820

Lick fraction decoding

Lick fraction decoding was performed using a neural network classification model (fitchet in MATLAB). The algorithm was trained per session for one second windows covering from -5 to + 10 sec in each trial. Only sessions with 16 or more trials were processed. The predicted stimulus was assessed using leave one trial out and winner takes all procedures.

Finally, while decoding accuracy for stimulus decoding did not differ substantially between decoding algorithms (Figure S5A), for lick decoding the algorithms that use nonlinear decoding (neural networks, NN and binary tree decision, BDT) performed substantially better than those that perform linear decoding (support vector machine, SVM, generalized linear model, GLM and linear discriminant analysis, LDA, Figure S5H) suggesting that decoding of lick behavior involves nonlinear neural activity interactions in dCA1 (GLM statistics for Figure S5H are shown in Data S1G).

Analysis of prediction shifts of S+ prediction for stimulus decoding between trials

Sudden changes in stimulus prediction from S- to S+ between trials were determined in
decoding prediction moving window averages (with windows of 10 time points) such as
the prediction time course shown in Figure 7A. We searched for a spontaneous shift in
prediction (arrow in Figure 7A) by searching for a sudden shift in prediction from below
the five percentile of the shuffled stimulus control for decoding prediction (lower edge of
the blue shade in Figure 7A) to above 95 percentile for the shuffled stimulus decoding
prediction (upper edge of the blue shade in Figure 7A). We compared the average time

courses for these spontaneous between-trial increases to S+ (spontaneous, cyan line in Figure 7F) to the time course of decoding prediction centered in the middle of adjacent between-trial intervals where we did not find a spontaneous increase to S+ (no change,

850

851

849

REFERENCES

magenta line in Figure 7F).

- Baker, K.L., Dickinson, M., Findley, T.M., Gire, D.H., Louis, M., Suver, M.P., Verhagen, J.V., Nagel, K.I., and Smear, M.C. (2018). Algorithms for Olfactory Search across Species. J Neurosci *38*, 9383-9389. 10.1523/JNEUROSCI.1668-18.2018.
- Losacco, J., Ramirez-Gordillo, D., Gilmer, J., and Restrepo, D. (2020). Learning improves decoding of odor identity with phase-referenced oscillations in the olfactory bulb. Elife *9*, e52583. 10.7554/eLife.52583.
- Wiltgen, B.J., Zhou, M., Cai, Y., Balaji, J., Karlsson, M.G., Parivash, S.N., Li, W., and Silva, A.J. (2010). The Hippocampus Plays a Selective Role in the Retrieval of Detailed Contextual Memories. Current Biology *20*, 1336-1344. https://doi.org/10.1016/j.cub.2010.06.068.
- Plitt, M.H., and Giocomo, L.M. (2021). Experience-dependent contextual codes in the hippocampus. Nature Neuroscience *24*, 705-714. 10.1038/s41593-021-00816-6.
- Stefanini, F., Kushnir, L., Jimenez, J.C., Jennings, J.H., Woods, N.I., Stuber,
 G.D., Kheirbek, M.A., Hen, R., and Fusi, S. (2020). A Distributed Neural Code in
 the Dentate Gyrus and in CA1. Neuron 107, 703-716.e704.
 https://doi.org/10.1016/j.neuron.2020.05.022.
- 871 6. Mau, W., Sullivan, D.W., Kinsky, N.R., Hasselmo, M.E., Howard, M.W., and 872 Eichenbaum, H. (2018). The Same Hippocampal CA1 Population Simultaneously 873 Codes Temporal Information over Multiple Timescales. Current Biology 28, 1499-874 1508.e1494. https://doi.org/10.1016/j.cub.2018.03.051.
- Buzsaki, G., and Moser, E.I. (2013). Memory, navigation and theta rhythm in the hippocampal-entorhinal system. Nat Neurosci *16*, 130-138. 10.1038/nn.3304.
- 8. Buzsáki, G., and Llinás, R. (2017). Space and time in the brain. Science *358*, 482-485. 10.1126/science.aan8869.

- Aery Jones, E.A., and Giocomo, L.M. (2023). Neural ensembles in navigation:
 From single cells to population codes. Current Opinion in Neurobiology 78,
 102665. https://doi.org/10.1016/j.conb.2022.102665.
- 10. Eichenbaum, H. (2017). On the Integration of Space, Time, and Memory. Neuron 95, 1007-1018. 10.1016/j.neuron.2017.06.036.
- Taxidis, J., Pnevmatikakis, E.A., Dorian, C.C., Mylavarapu, A.L., Arora, J.S., Samadian, K.D., Hoffberg, E.A., and Golshani, P. (2020). Differential Emergence and Stability of Sensory and Temporal Representations in Context-Specific Hippocampal Sequences. Neuron *108*, 984-998.e989. https://doi.org/10.1016/j.neuron.2020.08.028.
- Moser, E., Moser, M.B., and Andersen, P. (1993). Spatial learning impairment parallels the magnitude of dorsal hippocampal lesions, but is hardly present following ventral lesions. The Journal of Neuroscience *13*, 3916. 10.1523/JNEUROSCI.13-09-03916.1993.
- Strange, B.A., Witter, M.P., Lein, E.S., and Moser, E.I. (2014). Functional organization of the hippocampal longitudinal axis. Nature Reviews Neuroscience 15, 655-669. 10.1038/nrn3785.
- Rangel, L.M., Rueckemann, J.W., Riviere, P.D., Keefe, K.R., Porter, B.S., Heimbuch, I.S., Budlong, C.H., and Eichenbaum, H. (2016). Rhythmic coordination of hippocampal neurons during associative memory processing. Elife *5*. 10.7554/eLife.09849.
- 900 15. Biane, J.S., Ladow, M.A., Stefanini, F., Boddu, S.P., Fan, A., Hassan, S.,
 901 Dundar, N., Apodaca-Montano, D.L., Zhou, L.Z., Fayner, V., et al. (2023). Neural
 902 dynamics underlying associative learning in the dorsal and ventral hippocampus.
 903 Nature Neuroscience *26*, 798-809. 10.1038/s41593-023-01296-6.
- Li, Y., Xu, J., Liu, Y., Zhu, J., Liu, N., Zeng, W., Huang, N., Rasch, M.J., Jiang,
 H., Gu, X., et al. (2017). A distinct entorhinal cortex to hippocampal CA1 direct circuit for olfactory associative learning. Nature Neuroscience *20*, 559-570.
 10.1038/nn.4517.
- 908 17. MacDonald, C.J., Carrow, S., Place, R., and Eichenbaum, H. (2013). Distinct 909 Hippocampal Time Cell Sequences Represent Odor Memories in Immobilized 910 Rats. The Journal of Neuroscience 33, 14607. 10.1523/JNEUROSCI.1537-911 13.2013.
- 912 18. Shimbo, A., Izawa, E.-I., and Fujisawa, S. Scalable representation of time in the hippocampus. Science Advances *7*, eabd7013. 10.1126/sciadv.abd7013.
- 914 19. Singer, W., and Lazar, A. (2016). Does the cerebral cortex exploit high-915 dimensional, non-linear dynamics for information processing? Frontiers in 916 computational neuroscience *10*, 99.

- 917 20. Ma, M., Futia, G.L., de Souza, F.M.S., Ozbay, B.N., Llano, I., Gibson, E.A., and
- Restrepo, D. (2020). Molecular layer interneurons in the cerebellum encode for valence in associative learning. Nature Communications *11*, 4217.
- 920 10.1038/s41467-020-18034-2.
- 921 21. Li, X., Li, Y., Zhou, Y., Wu, J., Zhao, Z., Fan, J., Deng, F., Wu, Z., Xiao, G., He,
- J., et al. (2023). Real-time denoising enables high-sensitivity fluorescence time-
- lapse imaging beyond the shot-noise limit. Nature Biotechnology 41, 282-292.
- 924 10.1038/s41587-022-01450-8.
- 925 22. Pnevmatikakis, E.A., and Giovannucci, A. (2017). NoRMCorre: An online
- 926 algorithm for piecewise rigid motion correction of calcium imaging data. J
- 927 Neurosci Methods *291*, 83-94. 10.1016/j.jneumeth.2017.07.031.
- 928 23. Hakan, I., Claudia, S., Tugce, T., Biafra, O.A., Oscar, H., Jérôme, L., Fatih, D.,
- Mark, J.W., Murat, A.E., and Mark, J.S. (2021). Fast and statistically robust cell
- extraction from large-scale neural calcium imaging datasets. bioRxiv,
- 931 2021.2003.2024.436279. 10.1101/2021.03.24.436279.
- 932 24. Curran-Everett, D. (2000). Multiple comparisons: philosophies and illustrations.
- 933 Am.J.Physiol Regul.Integr.Comp Physiol 279, R1-R8.
- 934 25. Britten, K.H., Shadlen, M.N., Newsome, W.T., and Movshon, J.A. (1992). The
- analysis of visual motion: a comparison of neuronal and psychophysical
- 936 performance. J Neurosci *12*, 4745-4765.
- 937 26. Witter, M.P., Doan, T.P., Jacobsen, B., Nilssen, E.S., and Ohara, S. (2017).
- 938 Architecture of the Entorhinal Cortex A Review of Entorhinal Anatomy in Rodents
- with Some Comparative Notes. Frontiers in Systems Neuroscience 11.
- 940 27. Imai, T. (2014). Construction of functional neuronal circuitry in the olfactory bulb.
- 941 Seminars in Cell & Developmental Biology 35, 180-188.
- 942 https://doi.org/10.1016/j.semcdb.2014.07.012.
- 943 28. Igarashi, K.M., Lu, L., Colgin, L.L., Moser, M.-B., and Moser, E.I. (2014).
- 944 Coordination of entorhinal–hippocampal ensemble activity during associative
- 945 learning. Nature *510*, 143-147. 10.1038/nature13162.
- 946 29. Manns, J.R., Zilli, E.A., Ong, K.C., Hasselmo, M.E., and Eichenbaum, H. (2007).
- Hippocampal CA1 spiking during encoding and retrieval: relation to theta phase.
- 948 Neurobiol Learn Mem *87*, 9-20. 10.1016/j.nlm.2006.05.007.
- 949 30. Wood, E.R., Dudchenko, P.A., and Eichenbaum, H. (1999). The global record of
- 950 memory in hippocampal neuronal activity. Nature 397, 613-616. 10.1038/17605.
- 951 31. Radvansky, B.A., and Dombeck, D.A. (2018). An olfactory virtual reality system
- 952 for mice. Nat Commun 9, 839. 10.1038/s41467-018-03262-4.

- 953 32. Martinez, R.H., Lansner, A., and Herman, P. (2019). Probabilistic associative 954 learning suffices for learning the temporal structure of multiple sequences. PLOS 955 ONE *14*, e0220161. 10.1371/journal.pone.0220161.
- 956 33. Basu, J., and Siegelbaum, S.A. (2015). The corticohippocampal circuit, synaptic plasticity, and memory. Cold Spring Harbor perspectives in biology *7*, a021733.
- 958 34. Citri, A., and Malenka, R.C. (2008). Synaptic plasticity: multiple forms, functions, and mechanisms. Neuropsychopharmacology *33*, 18-41. 10.1038/sj.npp.1301559.
- 961 35. Fanselow, M.S., and Dong, H.-W. (2010). Are the Dorsal and Ventral Hippocampus Functionally Distinct Structures? Neuron *65*, 7-19. 10.1016/j.neuron.2009.11.031.
- 964 36. Sosa, M., and Giocomo, L.M. (2021). Navigating for reward. Nature Reviews Neuroscience *22*, 472-487. 10.1038/s41583-021-00479-z.
- 966 37. Martin, C., Beshel, J., and Kay, L.M. (2007). An olfacto-hippocampal network is dynamically involved in odor-discrimination learning. J.Neurophysiol. *98*, 2196-2205.
- Ramirez-Gordillo, D., Bayer, K.U., and Restrepo, D. (2022). Hippocampal Prefrontal θ Coupling Develops as Mice Become Proficient in Associative
 Odorant Discrimination Learning. eneuro 9, ENEURO.0259-0222.2022.
 10.1523/ENEURO.0259-22.2022.
- 2973 39. Libby, A., and Buschman, T.J. (2021). Rotational dynamics reduce interference between sensory and memory representations. Nature Neuroscience *24*, 715-726. 10.1038/s41593-021-00821-9.
- 976 40. Doucette, W., and Restrepo, D. (2008). Profound context-dependent plasticity of mitral cell responses in olfactory bulb. PLoS Biol *6*, e258. 08-PLBI-RA-1962 [pii] 978 10.1371/journal.pbio.0060258.
- Li, A., Gire, D.H., and Restrepo, D. (2015). Y spike-field coherence in a
 population of olfactory bulb neurons differentiates between odors irrespective of
 associated outcome. J Neurosci 35, 5808-5822. 10.1523/JNEUROSCI.4003 14.2015.
- 42. Abraham, N.M., Vincis, R., Lagier, S., Rodriguez, I., and Carleton, A. (2014). Long term functional plasticity of sensory inputs mediated by olfactory learning. Elife 3, e02109. 10.7554/eLife.02109.
- Chu, M.W., Li, W.L., and Komiyama, T. (2016). Balancing the Robustness and Efficiency of Odor Representations during Learning. Neuron *92*, 174-186. 10.1016/j.neuron.2016.09.004.

- 989 44. Stachenfeld, K.L., Botvinick, M.M., and Gershman, S.J. (2017). The 990 hippocampus as a predictive map. Nature Neuroscience *20*, 1643-1653. 991 10.1038/nn.4650.
- 992 45. Nieh, E.H., Schottdorf, M., Freeman, N.W., Low, R.J., Lewallen, S., Koay, S.A., Pinto, L., Gauthier, J.L., Brody, C.D., and Tank, D.W. (2021). Geometry of abstract learned knowledge in the hippocampus. Nature *595*, 80-84. 10.1038/s41586-021-03652-7.
- 996 46. Orhan, A.E., and Ma, W.J. (2019). A diverse range of factors affect the nature of neural representations underlying short-term memory. Nature Neuroscience *22*, 275-283. 10.1038/s41593-018-0314-y.
- 999 47. Feldman, J. (2013). The neural binding problem(s). Cognitive Neurodynamics *7*, 1000 1-11. 10.1007/s11571-012-9219-8.
- Hiratani, N., and Sompolinsky, H. (2023). Optimal quadratic binding for relational reasoning in vector symbolic neural architectures. Neural Computation *35*, 105-1003
- 1004 49. Dana, H., Chen, T.-W., Hu, A., Shields, B.C., Guo, C., Looger, L.L., Kim, D.S.,
 1005 and Svoboda, K. (2014). Thy1-GCaMP6 Transgenic Mice for Neuronal
 1006 Population Imaging In Vivo. PLOS ONE 9, e108697.
 1007 10.1371/journal.pone.0108697.
- 1008 50. Gire, D.H., Whitesell, J.D., Doucette, W., and Restrepo, D. (2013). Information for decision-making and stimulus identification is multiplexed in sensory cortex. Nat Neurosci *16*, 991-993. 10.1038/nn.3432.
- 51. Slotnick, B.M., and Restrepo, D. (2005). Olfactometry with mice. In Current
 1012 Protocols in Neuroscience, J.N. Crawley, C.R. Gerefen, M.A. Rogawski, D.R.
 1013 Sibley, P. Skolnick, and S. Wray, eds. (John Wiley and Sons, Inc), pp. 1-24
 1014
- Yu, Z., Guindani, M., Grieco, S.F., Chen, L., Holmes, T.C., and Xu, X. (2022).
 Beyond t test and ANOVA: applications of mixed-effects models for more rigorous statistical analysis in neuroscience research. Neuron *110*, 21-35. https://doi.org/10.1016/j.neuron.2021.10.030.
- Halsey, L.G., Curran-Everett, D., Vowler, S.L., and Drummond, G.B. (2015). The fickle P value generates irreproducible results. Nat Methods *12*, 179-185.
 1021 10.1038/nmeth.3288.

Table 1. Number of regions of interest per session used for analysis in the different figures.

| Figures | Mouse 1 | Mouse 2 | Mouse 3 | Mouse 4 | All mice |
|-----------------------------|----------------------|----------------------|-----------------------|-----------------------|-----------------------|
| Figures 2-4, Learning | 75 <u>+</u> 9, n=8 | 82 <u>+</u> 25, n=4 | 95 <u>+</u> 15, n=6 | n=0 | 83 <u>+</u> 17, n=18 |
| Figures 2-4, Proficiency | 79 <u>+</u> 12, n=14 | 96 <u>+</u> 25, n=10 | 108 <u>+</u> 18, n=22 | 178 <u>+</u> 23, n=20 | 121 <u>+</u> 43, n=66 |
| Figures 5-7 Learning | 75 <u>+</u> 9, n=8 | 82 <u>+</u> 25, n=4 | 96 <u>+</u> 14, n=7 | n=0 | 84 <u>+</u> 18, n=19 |
| Figures 5-7 Proficient | 73 <u>+</u> 10, n=9 | 96 <u>+</u> 25, n=10 | 104 <u>+</u> 15, n=20 | 177 <u>+</u> 23, n=19 | 122 <u>+</u> 45, n=58 |

The number of regions of interest per session (\pm S.D.) and the number of sessions (n) are shown for each figure/mouse

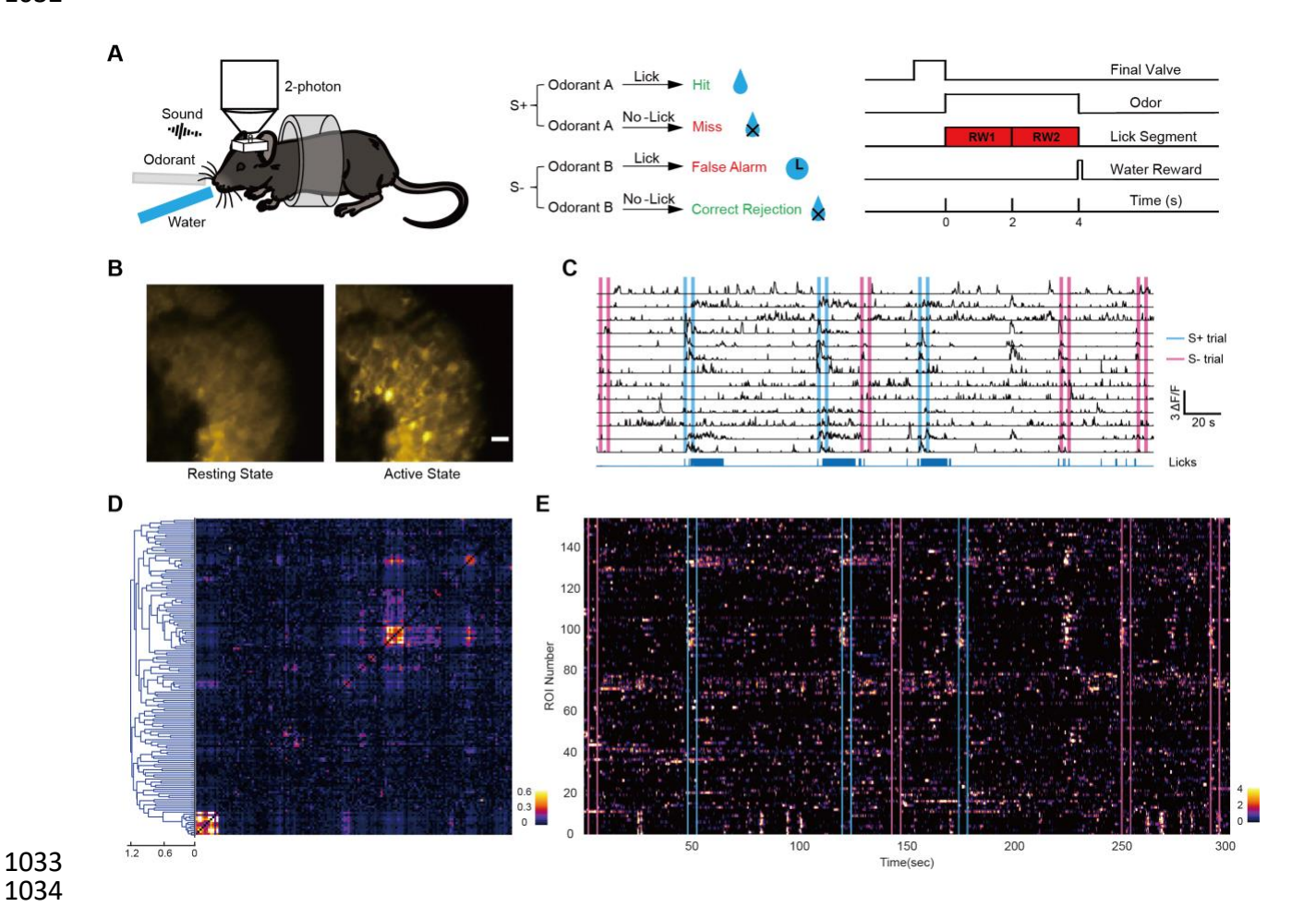


Figure 1. Two-photon Ca²⁺ imaging of stratum pyramidale cells in CA1 in head-fixed mice undergoing the go-no go associative learning task.

(A) Go-no go task. Left: Two-photon imaging of a head-fixed mouse responding to odorants by licking on a water spout in response to the rewarded odorant in the go-no go task. Center: Scoring of decision making. Right: Time course for the trial. In Hit trials, the animal must lick at least once in each of the two 2 second response window (RW) segments to receive a water reward as a reinforcement.

(B) Two-photon microscopy time-stacked images of GCaMP6f fluorescence recorded from SP cells in dCA1 through a GRIN lens in a proficient Thy1-GCaMP6f mouse engaged in the go-no go task. Left: Activity at rest. Right: Activity during the rewarded odorant trial. Video 1 shows fluorescence changes in this group of cells. (C) Δ F/F traces are shown for a subset of the regions of interest (ROIs) for the figure in B. The magenta vertical lines are the on and off times for the odorant in the unrewarded (S-) odorant trials and the cyan vertical lines are on and off times for the rewarded (S+) odorant. The blue lines at the bottom are lick recordings. (D) Cross-correlation and hierarchical clustering of the $\Delta F/F$ traces for 153 ROIs for the entire 20 minute session corresponding to B and C shows substantial heterogeneity in the calcium responses. (E) Pseudocolor plot of the time course for $\Delta F/F$ for the 153 hierarchically clustered ROIs.

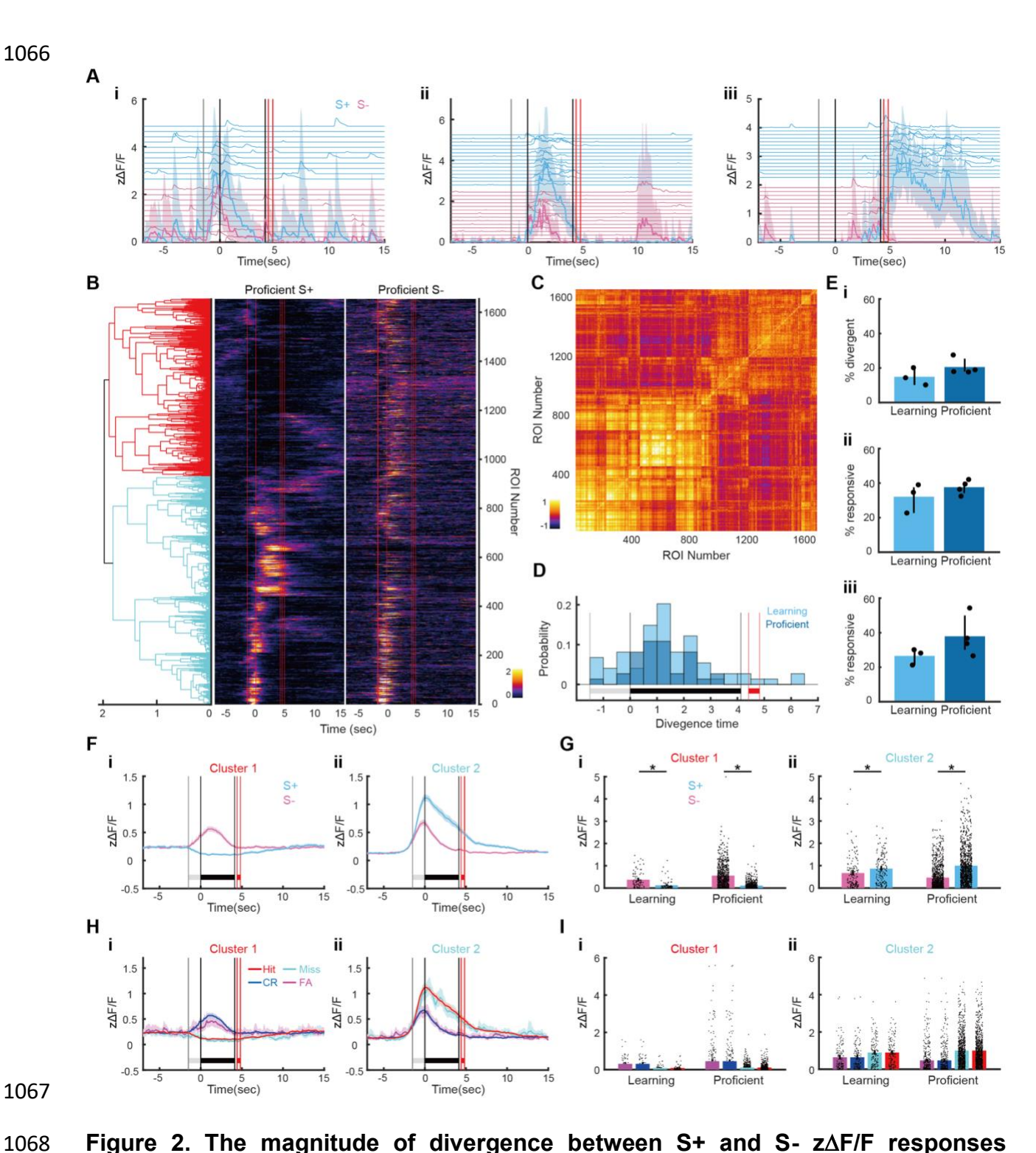


Figure 2. The magnitude of divergence between S+ and S- $z\Delta F/F$ responses increases with learning and the onset of divergence takes place at discrete times that differ between the learning and proficient stages.

(A) Examples of zΔF/F time courses for single ROIs that differ in onset time for divergence
 between S+ and S- trials. Selected ROIs with onset times (i) near the start of the trial, (ii)
 during odor presentation, and (iii) at reward delivery.

(B) Pseudocolor representation of $z\Delta F/F$ time courses for single ROIs that were divergent between S+ and S- trials in the proficient sessions (66 sessions, 4 mice). Time courses were sorted by estimating an agglomerative hierarchical cluster tree shown on the left. This tree was calculated using the cross-correlation coefficients between all divergent $z\Delta F/F$ S+ time courses shown in C. The red vertical lines show (in order): trial start, odorant on, odorant off, reinforcement on and reinforcement off.

1082 (C) Cross-correlation coefficients computed between all per trial $z\Delta F/F$ time courses shown in B. The coefficients were sorted by the agglomerative hierarchical cluster tree shown in B.

(D) Histograms for divergence times for all the ROIs for the proficient stage shown in B (dark blue) and for all divergent ROIs for learning stage sessions (light blue). Divergence time histograms are significantly different between learning and proficient (ranksum p<0.001, n=99 divergence time bins).

(E) i. Percent divergent ROIs per mouse. ii and iii. Percent responsive ROIs per mouse for S+ (ii) and S- (iii) trials. The percent divergent (i) and percent responsive (ii and ii)

differences between learning and proficient stages were not statistically significant (two tailed t test p>0.05, n=3 for learning and 4 for proficient, 5 d.f.). (F) Mean z∆F/F time courses for S+ and S- for the two clusters in the hierarchical tree shown in B. (G) Mean z∆F/F calculated per session in the time window from -0.5 to 0.5 sec for each cluster shown in F. (H) Mean $z\Delta F/F$ time courses for Hits (red), Miss (cyan), CRs (blue) and FAs (magenta) for the two clusters in the hierarchical tree shown in B. (I) Mean z∆F/F calculated per session in the time window from -0.5 to 0.5 sec for each cluster shown in H. Data S1A shows the GLM statistical analysis for Figures 2G and I. For all figures in the manuscript and for supplemental figures: The bounded lines such as those in A, F and H, represent the mean and 95% CI. The light grey horizontal bar is the period between the earliest trial start and odorant presentation (at 0 sec), the black horizontal bar is the time period for odorant presentation and the red horizontal bar is the

- period for water reward delivery. Vertical lines represent the earliest trial start, odorant valve opening and closing and reward valve opening and closing.



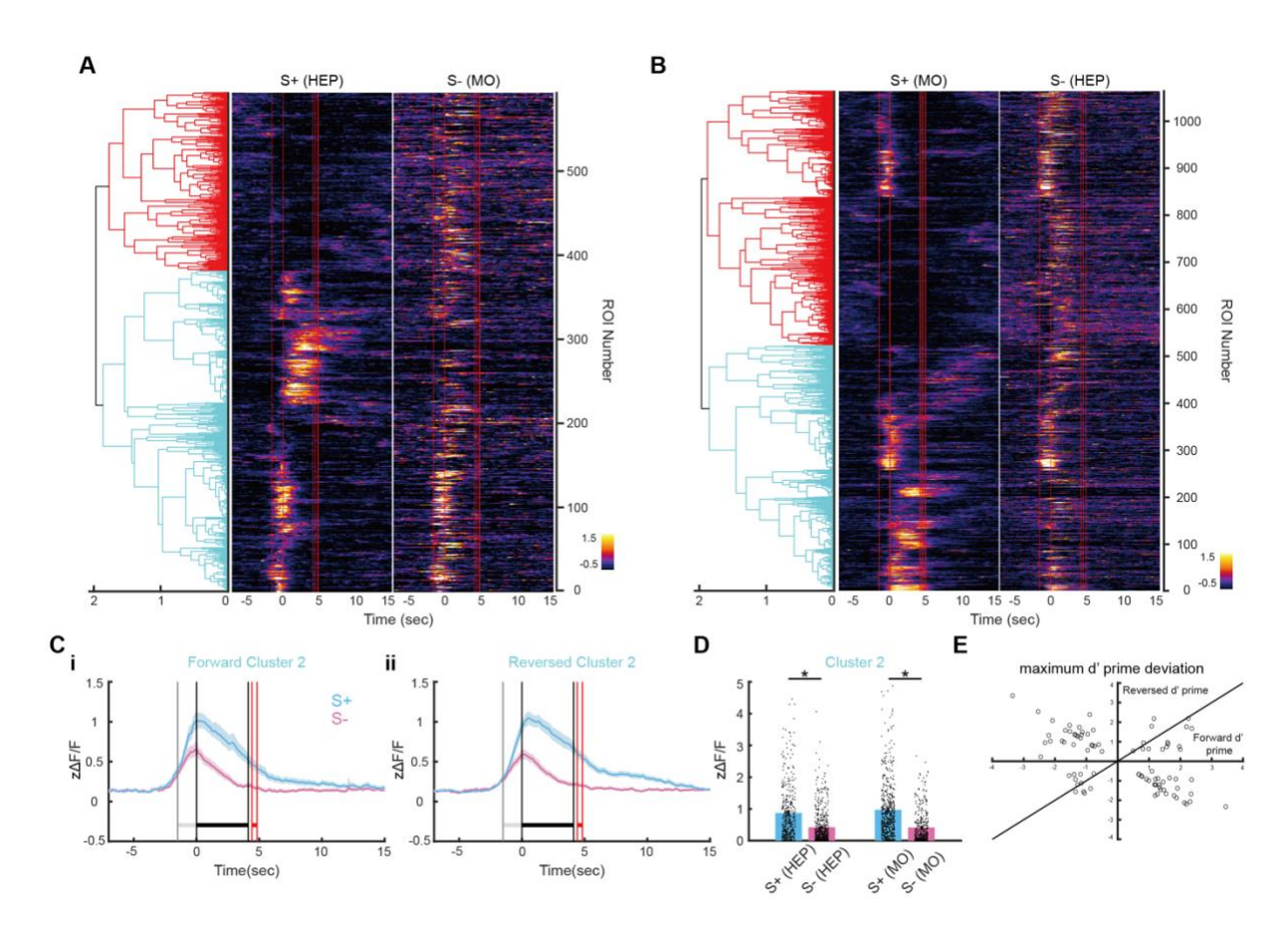


Figure 3. Reversal of odorant valence reveals that a substantial number of dCA1 cells respond to stimulus valence.

(A and B) $z\Delta F/F$ time courses for single ROIs that were divergent between S+ and S-trials for proficient mice. (A) shows $z\Delta F/F$ time courses for the forward proficient sessions where the rewarded odorant (S+) was HEP and the unrewarded odorant (S-) was MO (25 sessions, 4 mice) and (B) shows time courses for the reversed proficient sessions where the rewarded odorant (S+) was MO and the unrewarded odorant (S-) was HEP (41 sessions, 4 mice). For both A and B time courses were sorted by estimating an agglomerative hierarchical cluster tree shown on the left that was calculated using the

cross-correlation coefficients between all divergent z∆F/F time courses shown in Figure 1131 1132 S4B. The red vertical lines in A and B denote (in order): trial start, odorant on, odorant off, reinforcement on and reinforcement off. 1133 1134 (C) Mean $z\Delta F/F$ time courses for cluster 2 (blue cluster in A and B). Mean $z\Delta F/F$ time 1135 course for cluster 1 is shown in Figure S4. 1136 1137 (D) Mean $z\Delta F/F$ calculated per session in the time window from 1 to 2 seconds for cluster 1138 1139 2. Data S1B shows the GLM statistical analysis for these data. 1140 (E) Plot of peak d' values for z∆F/F time courses for a set of forward/reversed proficient 1141 1142 sessions where ROIs were matched from session to session in one mouse. The per ROI 1143 z∆F/F and d' time courses for these forward and reversed sessions are shown in Figure S4. The line shown is d' reversed = d' forward, which would be followed if the ROIs 1144 1145 represent stimulus identity.

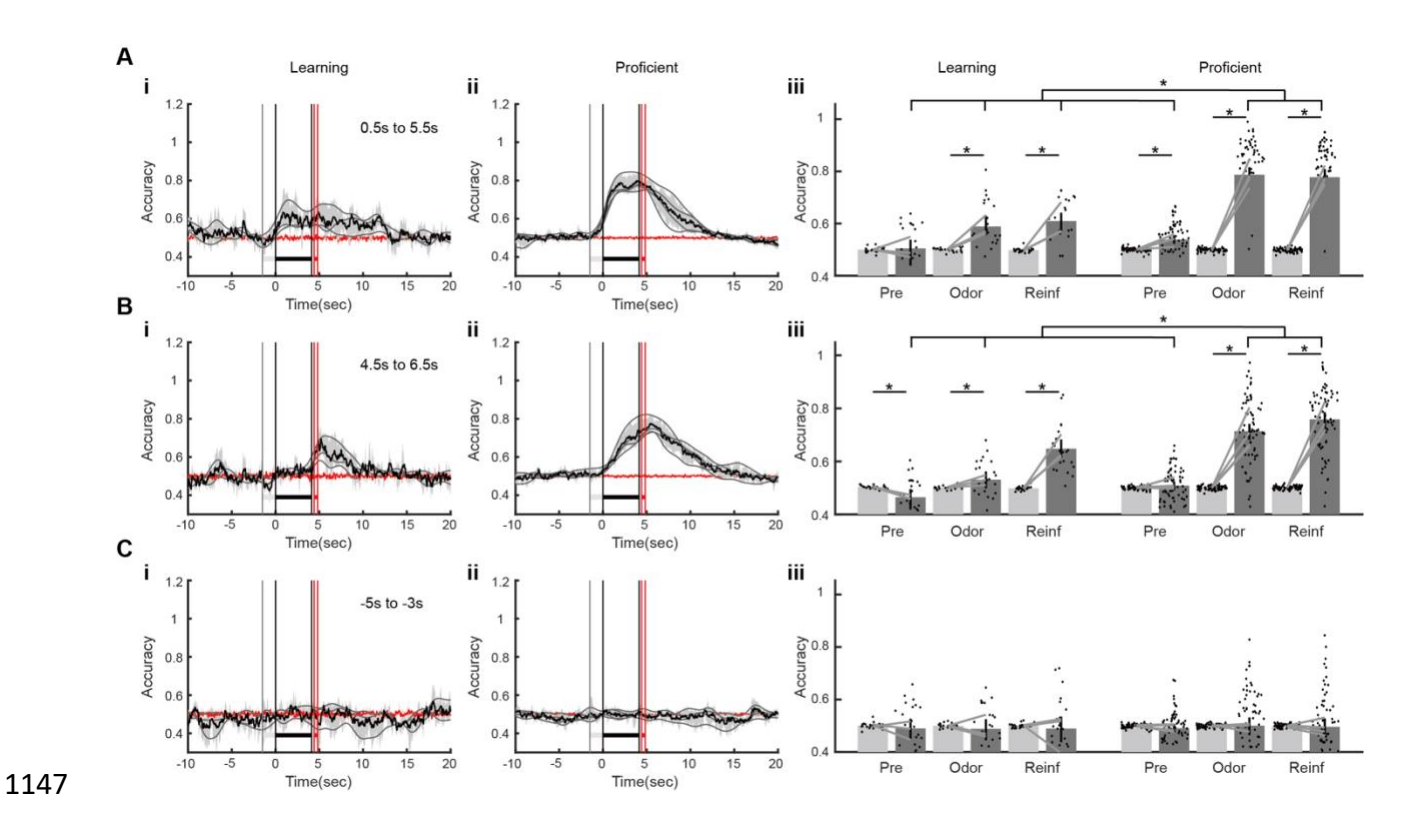


Figure 4. Learning elicits an increase in stimulus decoding accuracy.

(A to C). Each panel shows the accuracy of GLM decoding of the stimulus (S+ vs. S-) from per trial $z\Delta F/F$ responses for all trials and all ROIs per session for all learning stage sessions (i) and proficient sessions (ii) (4 mice, 18 learning sessions, 66 proficient sessions). The bounded black line represents the mean accuracy bounded by the 95% CI. The grey lines are per mouse accuracy. The red line is the stimulus decoding accuracy calculated after shuffling the stimulus labels (S+ vs S-). The bar graphs in iii show the mean accuracy for different trial periods (Pre-Odor -1 to 0, Odor 3.1 to 4.1 and Reinf 4.5 to 5.5). Light gray bars are the shuffled stimulus accuracies. Points are per

A to C differ by the time window used to train the GLM decoder.

session accuracies and bars are 95% Cls.

| 1161 | |
|------|---|
| 1162 | (A) The training window (0.5 to 5.5 sec) covers odorant presentation and reward |
| 1163 | delivery, |
| 1164 | |
| 1165 | (B) The training window included reward delivery (4.5 to 6.5 sec). |
| 1166 | |
| 1167 | (C) The training window takes place before trial start (-5 to -3 sec). |
| 1168 | |
| 1169 | |
| 1170 | |
| 1171 | |

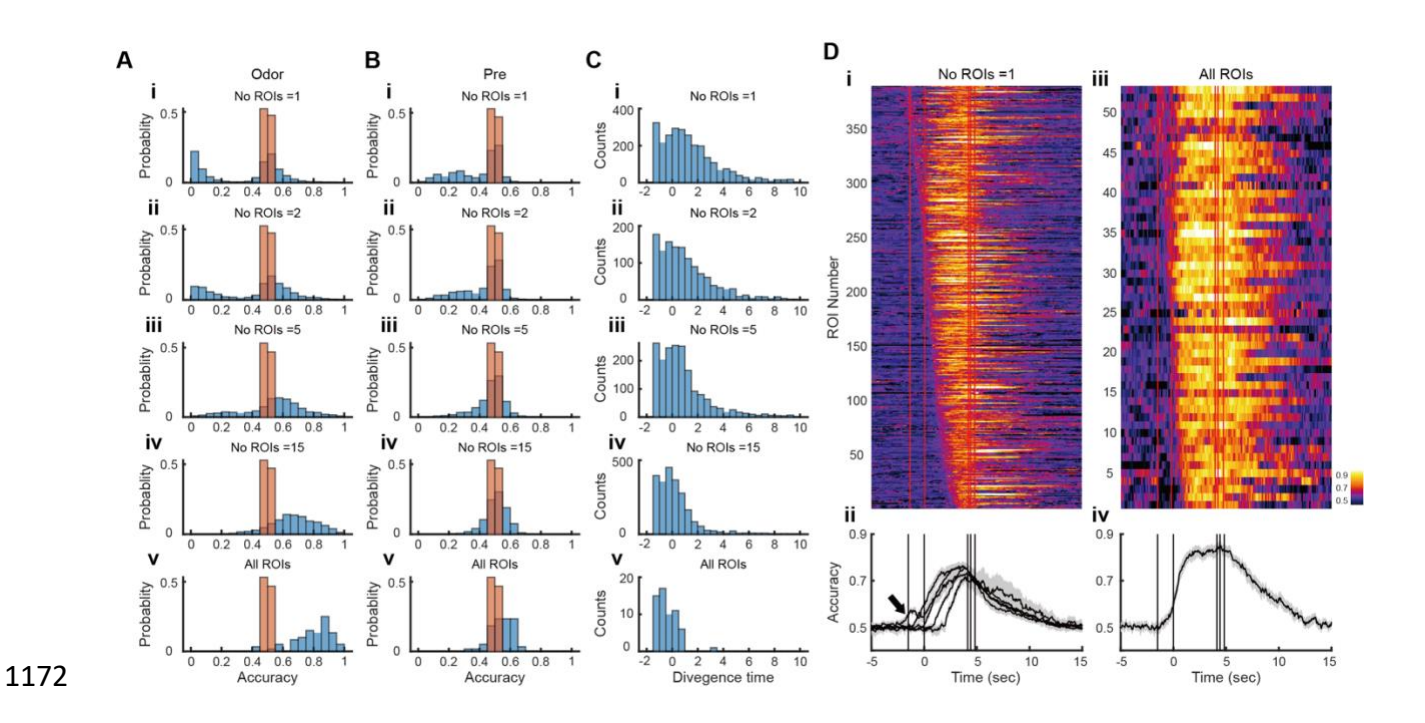


Figure 5. Stimulus decoding accuracy calculated per ROI for proficient animals reveals time tiling of the increase in stimulus decoding accuracy.

(A) Histogram for stimulus decoding accuracy calculated in the odor period (3.1 to 4.1 sec) for all proficient sessions (66 sessions) for 4 mice. i to v show the histogram for an increasing number of ROIs per decoding session. Blue is stimulus decoding accuracy, brown is stimulus decoding accuracy calculated after shuffling the labels. Histograms were normalized by dividing by the total number of counts.

(B) Histograms for stimulus decoding accuracy calculated in the Pre-Odor period (-1 to 0 sec). i to v show the histogram for an increasing number of ROIs per decoding session.

(C) Histograms for the onset of the increase in decoding accuracy for decoding runs that achieved at least 0.65 accuracy after trial start. i to v show the histogram for an increasing number of ROIs per decoding session.

(D) (i). Time courses for decoding accuracies calculated for a single ROI per session that reach at least 0.65 after trial start. (ii) Mean accuracy time courses calculated for one ROI accuracy time courses shown in Di with accuracy increase onsets in the following time periods: -1.5 to -1, -1 to 0, 0 to 1, 1 to 2, 2 to 3, >3 sec. (iii) Time courses for decoding accuracies calculated all ROIs per session. (iv) Mean accuracy time course for the time courses shown in Diii.

*p<0.05 for a pFDR-corrected t-test or ranksum tests, GLM statistics are in Data S1D. GLM analysis indicates that all histograms in A and B differ from each other, and all histograms in C differ from each other (Data S1D).

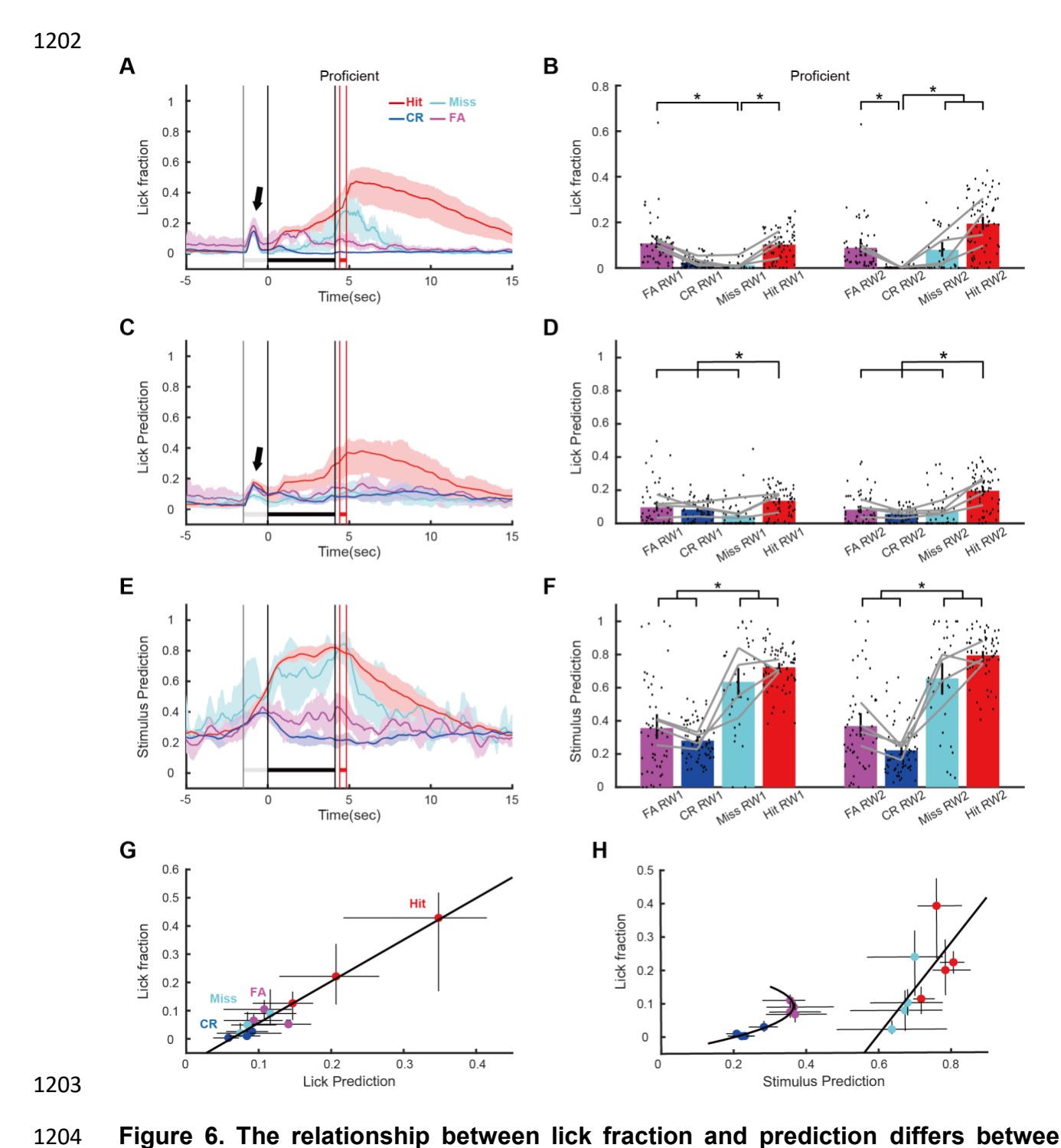


Figure 6. The relationship between lick fraction and prediction differs between stimulus decoding and decoding of lick fraction.

1207 (A) Mean lick fraction time course calculated for hits (red), Miss (cyan), correct rejections 1208 (CR, blue) or false alarm (FA, magenta) trials for all sessions when the mice were 1209 proficient (66 sessions, 4 mice). 1210 (B) Bar graph quantifying mean lick fraction for proficient mice (66 sessions, 4 mice) in 1211 1212 the two 2 second response windows of the odor period where the mouse must lick at least 1213 once to get water in a Hit trial (Figure 1A). Dots are per session lick fraction and grey 1214 lines are per mouse averages. 1215 (C) Mean prediction time course for lick fraction decoding within trials calculated for hits 1216 1217 (red), Miss (cyan), correct rejections (CR, blue) or false alarm (FA, magenta) trials for all sessions when the mice were proficient (66 sessions, 4 mice). 1218 1219 (D) Bar graph quantifying mean lick fraction prediction for proficient mice (66 sessions, 4 1220 1221 mice) in the two 2 second response windows of the odor period where the mouse must 1222 lick at least once to get water in a Hit trial (Figure 1A). Dots are per session prediction 1223 and grey lines are per mouse averages. 1224 1225 (E) Mean stimulus prediction time course within trials calculated for hits (red), Miss (cyan), 1226 correct rejections (CR, blue) or false alarm (FA, magenta) trials for all sessions when the

1227

1228

mice were proficient (66 sessions, 4 mice).

(F) Bar graph quantifying mean stimulus prediction for proficient mice (66 sessions, 4 mice) in the two 2 second response windows of the odor period where the mouse must lick at least once to get water in a Hit trial (Figure 1A). Dots are per session prediction and grey lines are per mouse averages. The training period for the GLM decoding algorithm was 0.5 to 5.5 sec.

(G) Relationship between mean lick fraction and mean lick fraction prediction (calculated with per mouse values). The bars are 95% CIs calculated per mouse. Lick fraction and lick fraction prediction were calculated in two second time windows spanning from odor onset to 6 sec after odor onset. The line is a linear fit.

(H) Relationship between mean lick fraction and mean stimulus prediction (calculated from per mouse values). The bars are 95% CIs calculated per mouse. Lick fraction and stimulus prediction were calculated in two second time windows spanning from odor onset to 6 sec after odor onset. Lines are a linear fit of the data for Hit and Miss and a second order polynomial fit for CR and FA.

For the graphs the data are shown separately for S+ Hits (red) and Miss (cyan) and S-CR (blue) and FA (magenta) trials. *p<0.05 for a pFDR-corrected t-test or ranksum tests, GLM statistics are in Data S1E.

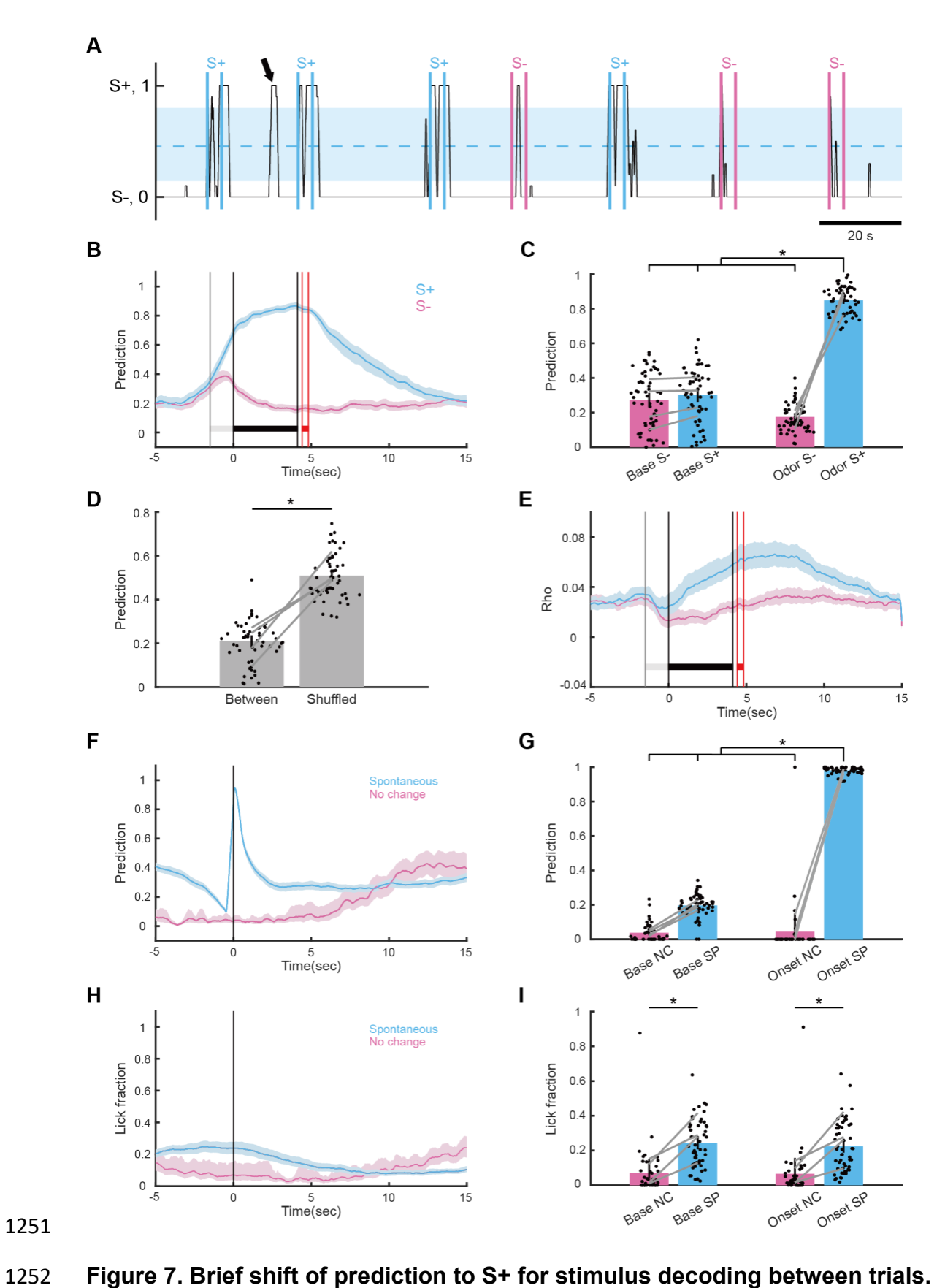


Figure 7. Brief shift of prediction to S+ for stimulus decoding between trials.

(A) Example of the time course for stimulus decoding prediction during a session when
the animal was proficient in the go-no go task. Prediction ranges from 0 (S-) to 1 (S+).

Cyan vertical bars are the odor on and odor off times for the S+ trials and magenta vertical
bars are the odor on and odor off times for the S- trials. The shaded blue area is the 5 to
95 percentile decoding prediction calculated for decoding with shuffled trial labels. The
arrow points to a sudden shift in prediction above the shuffled 95 percentile that took
place between trials (we call this a prediction shift).

(B) Mean stimulus prediction time course within trials calculated for S+ and S- trials for all sessions when the mice were proficient (66 sessions, 4 mice).

(C) Bar graph quantifying mean label prediction for S+ and S- trials in two time windows:

Base (-2.5 to -1.5 sec) and odor (2 to 4.1 sec). Dots are per session mean label prediction

and grey lines are per mouse mean label prediction.

(D) Bar graph quantifying the mean label prediction between trials compared to the mean label prediction between trials for shuffled label decoding.

(E) Correlation between label prediction calculated at each time point in the prediction time course for all S+ or S- trials within a session and the label prediction value found at the point of spontaneous shift for spontaneous shifts in prediction found in between trials in the same session (66 sessions, 4 mice).

| 1276 | |
|------|--|
| 1277 | (F) Mean label prediction time course for between-trial spontaneous prediction shifts |
| 1278 | ("spontaneous") and for time courses in between trials periods where we did not find |
| 1279 | spontaneous shifts to S+ ("no change") (66 sessions, 4 mice). |
| 1280 | |
| 1281 | (G) Bar graph quantifying mean label prediction for between-trial spontaneous prediction |
| 1282 | shifts and for no change between-trial prediction time courses calculated in two time |
| 1283 | windows: Base (-2.5 to -1.5 sec) and odor (2 to 4.1 sec). Dots are per session mean label |
| 1284 | prediction and grey lines are per mouse mean label prediction. |
| 1285 | |
| 1286 | (H) Mean lick fraction time course for between-trial spontaneous prediction shifts |
| 1287 | ("spontaneous") and for time courses in between trials periods where we did not find |
| 1288 | spontaneous shifts to S+ ("no change") (66 sessions, 4 mice). |
| 1289 | |
| 1290 | (I) Bar graph quantifying mean lick fraction for between-trial spontaneous prediction shifts |
| 1291 | and for no change between-trial prediction time courses calculated in two time windows: |
| 1292 | Base (-2 to -0 sec) and odor (0 to 2 sec). Dots are per session mean lick fraction and grey |
| 1293 | lines are per mouse mean lick fraction. |
| 1294 | |
| 1295 | |
| 1296 | |
| 1297 | *p<0.05 for a pFDR-corrected t-test or ranksum tests, GLM statistics are in Data S1F. |
| 1298 | |